

Active strain-sensing with a nanoporous-metal hybrid material

**Vom Promotionsausschuss der
Technischen Universität Hamburg**
zur Erlangung des akademischen Grades
Doktorin der Naturwissenschaften (Dr. rer. nat.)

genehmigte Dissertation

von

Charlotte Uta Beate Kuss

aus

München

2019

Gutachter der Dissertation:

Prof. Dr.-Ing. Jörg Weissmüller, Technische Universität Hamburg

Prof. Dr. rer. nat. Gerold Schneider, Technische Universität Hamburg

Vorsitzender des Prüfungsausschusses:

Prof. Dr.-Ing. Robert Meißner, Technische Universität Hamburg

Datum der Disputation:

22. Oktober 2019

Acknowledgements

I would like to express my deep gratitude to all the people who supported me throughout the very special and exciting time of my phd studies.

First of all, I am very grateful to the mentor of my thesis Prof. Jörg Weissmüller, who gave me the opportunity to work on such a fascinating topic; I could always rely on his support and enthusiasm for my research. As a mother (-to-be) he enabled and encouraged me to finish my work under his supervision.

Dr. Jürgen Markmann, my office-roommate on fridays, was a great support not only by patiently discussing with me, but I also benefited from his great insight into measurement electronics.

I want to thank Prof. Gerold Schneider for being the second reviewer and Prof. Robert Meißner for being the chairman of the disputation.

I was extremely lucky to work in such a great environment, with state-of-the-art-equipment and colleagues that always supported me and made me get up and got to work every day.

First of all I'd like to thank Nadiia Mameka and Lihua Shao who helped me from the very beginning, without both I would not have started so smoothly. Lukas Lühns supported me not only in scientific questions but also during teaching students in materials sciences. It has been a pleasure working with Mark Busch, Benedikt Roschning, Birthe Zandersons, Qibo Deng, Shan Shi, Nam Ngo, and Dr. Robert Günther, I am very grateful for your support and the good times we had together.

I want to thank Haide Alfort-Springer for baby-sitting on various occasions and her continuous support throughout the whole time of my phd. For help in technical matters I thank Claudia Plaumann, Claudia Karduck (you will not be forgotten), and Rainer Behn. Last but not least I am deeply grateful for the huge support from my family and friends, especially from my husband Thimo Kuss who always believed in me.

Abstract

Via impregnating a nanoporous metal with a liquid ionic conductor (electrolyte) a hybrid material with two capacitively connected charge-transport paths is created. Thus, space-charge layers along the large internal interface of the hybrid material are coupled to electric potential differences between the phases. The space charge is connected to mechanical deformation of the hybrid material via electrocapillary coupling.

In this work *active strain-sensing* with a nanoporous-metal electrolyte hybrid material is presented for the first time: Via cyclic deformation of the macroscopic body particularly robust potential- and current responses can be obtained. The investigated hybrid material exhibits a large longitudinal charge-load coupling parameter $dQ/dF|_E$, which is determined as $1.5 \mu\text{C N}^{-1}$ under quasi-static conditions. Furthermore, a quantitative analysis of the results via the effective potential-strain coupling parameter, ζ^* , is given for this type of material. ζ^* is linked thermodynamically to an electromechanical coupling parameter for actuation and to elastic properties of the material. This relation, derived from phenomenological thermodynamics in this work, leads to good agreement between experiment and theory. The potential-strain coupling parameter, which is experimentally determined as $\zeta^* = -50 \text{ mV}$, is even exploited to gain insight into the microscopic deformation mechanisms. Furthermore, the influence of network features, such as structure size, are investigated and indicate a decrease of ζ^* with increase in structure size.

All experiments were performed in an *in situ* electrochemical cell implemented in a dynamic mechanical analyzer, especially designed for sensing measurements on volumetric nanoporous metal-electrolyte hybrid materials. The experiments show that this class of material behaves phenomenologically equally to piezoceramics although the underlying microscopic mechanisms are completely different.

Kurzbeschreibung

Durch das Tränken der Poren eines nanoporösen Metalls mit einem flüssigen Ionenleiter (Elektrolyt) entsteht ein Hybridmaterial mit zwei kapazitiv verbundenen Ladungstransportpfaden. Die Raumladungsschichten entlang der großen inneren Grenzfläche des Hybridmaterials sind mit elektrischen Potentialunterschieden zwischen den Phasen gekoppelt. Die Raumladung ist mit der mechanischen Verformung des Hybridmaterials über Elektrokapillarkopplung verbunden.

In dieser Arbeit wird zum ersten Mal *aktive Dehnungs-Sensorik* mit einem nanoporösen Metallelektrolyt-Hybridmaterial gezeigt: Durch zyklische Verformung der makroskopischen Probe können robuste Potential- und Stromsignale erzeugt werden. Das untersuchte Hybridmaterial zeigt einen großen longitudinalen Ladungs-Last-Kopplungsparameter $dQ/dF|_E$, der als $1.5 \mu\text{C N}^{-1}$ unter quasistatischen Bedingungen bestimmt wird. Darüber hinaus wird eine quantitative Analyse der Ergebnisse mittels des effektiven Potential-Dehnungs-Kopplungsparameter ζ^* gegeben. ζ^* ist thermodynamisch mit einem elektromechanischen Kopplungsparameter für Aktorik und den elastischen Eigenschaften des Materials verknüpft. Diese Beziehung, abgeleitet in dieser Arbeit aus der phänomenologischen Thermodynamik, zeigt eine gute Übereinstimmung zwischen Experiment und Theorie. Der Potential-Dehnungs-Kopplungsparameter, experimentell als $\zeta^* = -50 \text{ mV}$ bestimmt, wird auch genutzt, um Einblicke in die mikroskopischen Verformungsmechanismen zu erhalten. Darüber hinaus wird der Einfluss von Netzwerkeigenschaften wie Strukturgröße untersucht; eine Abnahme von ζ^* mit zunehmender Strukturgröße wird beobachtet.

Alle Experimente wurden mittels einer in einer dynamischen mechanischen Analyse in einer implementierten elektrochemischen Zelle durchgeführt, die speziell für die Messung von volumetrischen nanoporösen Metallelektrolyt-Hybridmaterialien entwickelt wurde. Die Experimente zeigen, dass sich die Materialklasse aus Metall-Elektrolyt Hybridmaterialien phänomenologisch wie die Klasse der Piezokeramiken verhält, obwohl die zugrunde liegenden mikroskopischen Mechanismen völlig verschieden sind.

Contents

List of Figures	xi
List of Tables	xiii
1 Introduction	1
1.1 Nanoporous metals and piezoceramics - phenomenologically equal?	1
1.2 Research aims and experimental approaches	5
1.3 Outline of thesis	5
2 Theory	7
2.1 Fundamentals of electrochemistry	7
2.1.1 Electrochemical cell	7
2.1.2 The ideal polarized electrode and electrical double layer	7
2.1.3 Faradaic and capacitive processes	9
2.2 Electromechanical coupling	10
2.2.1 Thermodynamics of electrodes	10
2.2.2 Electromechanical coupling parameter	11
2.2.3 Nanoporous metal networks as electrodes and their electromechanical coupling	13
3 Experimental	17
3.1 Nanoporous gold	17
3.2 Measurement techniques	18
3.2.1 Three electrode setup	18
3.2.2 Reference electrodes	19
3.2.3 Chronoamperometry	20
3.2.4 Cyclic voltammetry	21
3.2.5 Impedance spectroscopy	22
3.2.6 Fundamentals of Lock-In amplifiers	26
3.2.7 Dynamic mechanical analysis	27
3.3 Sample preparation	29
3.3.1 Master alloy preparation and dealloying	29
3.3.2 Electrochemical and thermal annealing	30
3.4 Measurement setup	31
3.4.1 Determination of surface area	34
3.4.2 Sensing experiments	34
3.4.3 Actuation experiments	36
3.4.4 Machine stiffness	37

4	Results	39
4.1	Thermodynamical description of the system	39
4.1.1	Sensing-actuation relation	39
4.1.2	Charge-load coupling parameter and the corresponding piezoelectric coefficient	40
4.2	Experimental results	43
4.2.1	Actuation with nanoporous gold	43
4.2.2	Strain-sensing with nanoporous gold: Proof of principle	46
4.2.3	Strain-sensing with different strain amplitudes	47
4.2.4	Dependence of potential- and current responses on strain-frequency	49
4.2.5	Charge-load coupling at finite and quasi-static frequencies	52
4.2.6	Dependence of potential- and current responses on connectivity density and ligament size	53
5	Discussion	57
5.1	Quantification of sensing-actuation relation	57
5.2	Sensing efficiency of nanoporous-metal electrolyte hybrid materials	58
5.3	Local and macroscopic strain	60
6	Summary and Outlook	65
	References	68

List of Figures

1.1	Electrochemical responses of a planar gold electrode to cyclic strain	1
1.2	Actuation with a nanoporous metal-electrolyte hybrid material	3
1.3	Schematic of actuation with a piezoceramic material	4
2.1	The electrochemical double layer	8
2.2	Microscopic origin of surface stress	12
2.3	Schematic of sensing and actuation mechanism of a nanoporous hybrid-material	14
3.1	Nanoporous gold, an interconnected network of ligaments	17
3.2	Three electrode setup of an electrochemical cell	19
3.3	Offset of silver silver-chloride quasi reference electrode (Ag/AgCl) compared to a standard hydrogen electrode	20
3.4	Chronoamperometry on an ideally polarizable electrode	20
3.5	Cyclic voltammogram of a nanoporous gold specimen	22
3.6	<i>Randles equivalent circuit</i> of electrochemical cell	23
3.7	Complex-plane plots of equivalent circuit at high frequencies and nanoporous gold	24
3.8	Representative potential and current signals obtained via the impedance spectroscopy module	25
3.9	Block diagram of Lock-In amplifier	26
3.10	Dynamic mechanical analysis setup and representative measurements . . .	28
3.11	Electrochemical setup for dealloying	29
3.12	Dynamic mechanical analyzer setup for <i>in situ</i> electrochemical measurements	32
3.13	Load-unload curve of nanoporous gold specimen	33
3.14	Cyclic voltammograms to determine the quasi-static capacity and the surface area	34
3.15	Schematic of <i>in situ</i> sensing measurement setup	35
3.16	Determination of machine stiffness	37
4.1	Actuation measurements performed on nanoporous gold	44
4.2	Determination of effective strain-charge coefficient A^*	45
4.3	Strain-sensing measurement signals obtained via an oscilloscope	46
4.4	Determination of effective potential-strain coupling parameter ζ^*	48
4.5	Dynamic mechanic analysis measurements performed at constant effective strain amplitude $\hat{\epsilon}^*$	49
4.6	Frequency dependence of potential response at constant strain amplitude .	50
4.7	Frequency dependence of current response at constant strain/potential amplitude	51

4.8	Frequency dependence of charge response at constant strain/potential amplitude	52
4.9	Quasi static sensing experiment for determination of coupling of net charge on the sample and external load	53
4.10	Scanning electron micrograph of nanoporous gold samples with different ligament sizes and network connectivity densities	54
4.11	Dependence of potential and current response on ligament size and network connectivity density	55
5.1	Comparison the charge-load response of nanoporous gold- based hybrid material to that of lead zirconium titanate	59
6.1	Tuning the actuation efficiency of a nanoporous metal via polypyrrol coating	66

List of Tables

5.1	Effective potential-strain coupling parameters obtained via sensing and actuation measurements	58
5.2	Effective potential-strain coupling parameters for specimens of different connectivity densities and ligament sizes	63

1 Introduction

1.1 Nanoporous metals and piezoceramics - phenomenologically equal?

By immersing a material into an aqueous ionic conductor (electrolyte) a solid-liquid interface is created. In electrochemistry, such interface is called an electrode surface. For metals, such as gold or platinum, the electrode surface can be polarized and exhibits a capacitance depending on the surface area of the electrode. The coupling phenomena in metal-electrolyte interfaces connect capillary forces to the electric potential of the metal surface as stated in Refs. [1, 2]. Due to this coupling mechanical deformation changes the potential or charge of the electrode. In previous publications the electromechanical coupling of planar gold electrodes to surface strain has been investigated [3–5].

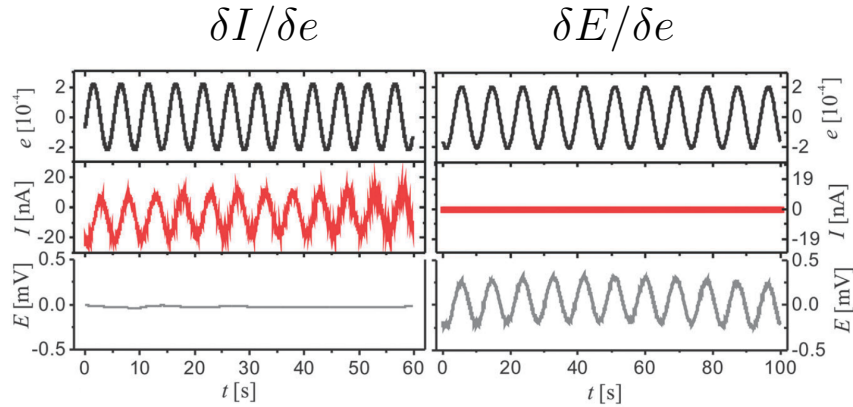


Figure 1.1: Electrochemical responses of a planar gold electrode to cyclic strain. $\delta I/\delta e$: While keeping the potential, E , constant, (*below*) a current response, I , (*middle*) to an applied cyclic strain, e , (*above*) can be observed. Inversely ($\delta E/\delta e$), a potential response, E , (*below*) is induced by a cyclic strain (*above*), when keeping the charge constant, i.e. $I = 0$, *middle*. Reproduced from [5] with permission from the PCCP Owner Societies.

A representative result is depicted in Fig. 1.1: Via applying a sinusoidal strain, $e(t)$, to the gold electrode a current response, $I(t)$, i.e. displacement of charge, was obtained if the potential, E , was held constant (see $\delta I/\delta e$). If the charge is kept constant, i.e. $I = 0$, the electrode responds to strain via a potential variation (see $\delta E/\delta e$). The efficiency of

the capillary coupling on planar electrodes is quantified by the potential-strain response parameter $\varsigma = dE/de|_q$, which yields -2.0 V for gold in experiments and simulation [5,6]. Via increasing the surface area of the metal electrode a higher capacitance and more available sites for chemical reactions can be achieved. A possibility to obtain a larger surface area is to prepare nanoporous metals, which also exhibit further beneficial properties and a straightforward synthesis procedure as described in the following:

Nanoporous-metal specimens consisting of a uniform network of nanometer-sized “ligaments” can be synthesized via dealloying, i.e. removing one or more components of an alloy [7–9]. Such nanoporous bodies are monolithic, have macroscopic dimensions of mm or cm, and exhibit good mechanical properties [10]. The ligaments can achieve dimensions down to 5 nm [11,12]. Thus, nanoporous metals consist of an extremely large internal surface and exhibit a high surface area-to-volume ratio. The specimens in this work displayed a surface area-to-volume ratio, which is indicated by the specific surface area, α , of $\approx 6 \times 10^7 \text{ m}^{-1}$ or the surface area per mass ratio, α_M , of $\approx 11 \times 10^5 \text{ m kg}^{-1}$. Therefore, in such porous materials the contribution of surface area plays an important role regarding the behavior of the macroscopic body [13]. By imbibing nanoporous metals with an electrolyte an electrolyte-metal hybrid material containing huge internal surfaces which are separated by only a few nm can be created [14]. Polarizable sites are almost homogeneously distributed at the interface of the hybrid material.

An equivalent behavior as observed at planar gold electrodes is expected from a nanoporous gold-electrolyte hybrid material: By exposing a macroscopic sample to an effective strain, ε^* , charge accumulates at the surface (at constant potential) or a potential variation can be detected (at open circuit and constant charge). However, the microscopic picture of this effect, i.e. the coupling between effective strain and the local strain field on the ligaments is under discussion (see Refs. [10,15,16]).

Besides the coupling phenomenon leading to strain-sensing, nanoporous metal-electrolyte hybrid materials attract attention in the community of electrochemists concerning catalysis, e.g. the catalytic oxidation of carbon monoxide (CO) with molecular oxygen (O_2) [17–19] or methanol oxidation [20]. Moreover, it was found out that via changing the surface charge density of a nanoporous-metal electrode, one can indeed observe resulting elastic strain, ε^* , induced by a capillary force [1,2,21]. The first experimental demonstration of this connection via electrochemical actuation exploited nanoporous platinum samples prepared by solidifying platinum nanoparticles. Figure 1.2 a) shows a scanning electron micrograph of the structure, whereas b) sketches the metal surface, which is polarized against the surrounding electrolyte. Strain amplitudes in the order of 0.1% were reported [14]. A few years later, reversible strain amplitudes in excess of 1% were achieved in similar measurements using nanoporous metals prepared by dealloying [12]. Further-

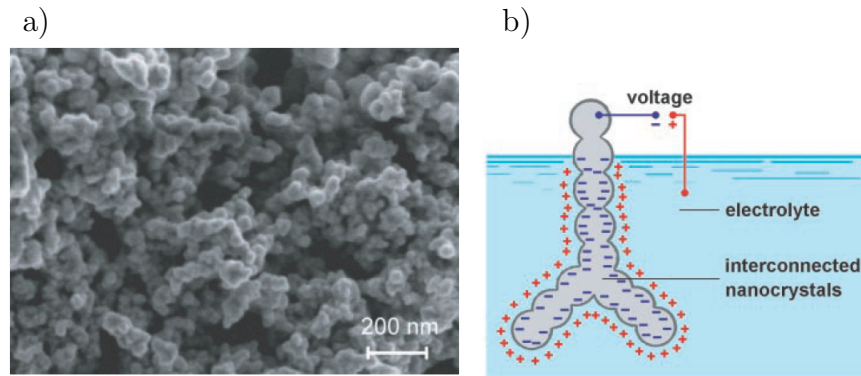


Figure 1.2: Actuation with a nanoporous metal-electrolyte hybrid material. a) shows a scanning electron micrograph of a fracture surface of nanoporous platinum. The nanoparticles as well as the pore-space are interconnected. A schematic of the structure imbibed with electrolyte is depicted in b). Reprinted from Weissmüller *et al.*, *Science*, 300(5617):312-315, 2003. Reprinted with permission from AAAS.

more, the actuation ability of a nanoporous material could be improved by covering the metal skeleton with a conducting polymer. Two examples will be mentioned here exemplarily: Polyaniline (PANI) lead to an improvement by a factor of three compared to the nanoporous gold skeleton exploited in the same work [22] or polypyrrol (PPy) increased the performance more than tenfold [23]. These experiments, among others, employ the above-mentioned polarization of metal-electrolyte interfaces. The surface stress is changed by polarization and therefore the material responds to potential variation by macroscopic expansion or contraction [12, 14, 24–26].

However, the most common and widely discussed sensor/actuator materials are piezoceramics, such as quartz (SiO_2) or lead zirconium titanate, ($\text{Pb}(\text{Zr},\text{Ti})\text{O}_3$, PZT). Since the discovery of piezoelectricity in the end of the nineteenth century piezoelectricity is a very relevant topic in science and piezoceramics are found in various applications. In 2007, for example, the *Guide to Literature of Piezoelectricity and Pyroelectricity*, which is a bibliography that contains references published during 2004 and 2005 on piezoelectric and pyroelectric materials and their applications, listed 2235 journal articles, patents, and dissertations [27].

Piezoelectricity is distinguished in two phenomenons, the piezoelectric and the *converse* piezoelectric effect. The latter effect corresponds to actuation phenomena, i.e. stress or deformation under an applied electric field/charging [28].

Figure 1.3 depicts a schematic of the piezoelectric effect: The ability of a material to develop electric displacement as a result of an applied mechanical stress. The name derives from the combination of the greek terms “piezo” ($\pi\acute{\epsilon}\zeta\omega$) or “piezein” ($\pi\acute{\epsilon}\zeta\epsilon\iota\eta$), which means to squeeze or to press, and from “electric” or “electron” ($\acute{\eta}\gamma\epsilon\kappa\tau\rho\nu$) whose literal translation is amber, an ancient source of electric charge [30]. In piezoelectric crystals,

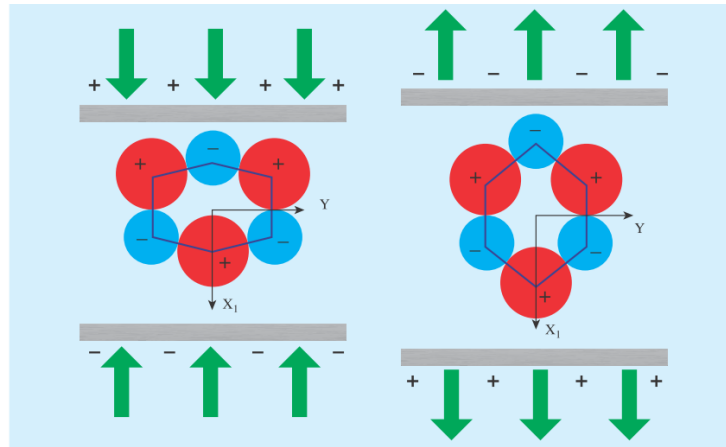


Figure 1.3: Schematic of actuation with a piezoceramic material. Illustration of the piezoelectric effect in a quartz crystal, SiO_2 . Si-atoms exhibit a lower electronegativity than O_2 -molecules resulting in dipoles with charges that are compensated by the crystal lattice. Si-atoms (O_2 -molecules) are indicated by red (blue) circles and furnished with a “+” (“-”) sign to demonstrate the charge, respectively. Charges at the surfaces are induced due to mechanical compressive (*left*) and tensile deformation (*right*) depicted by the green arrows along the electrical X_1 -axis. Schematics reprinted from Ref. [29] ©IOP Publishing. Reproduced with permission. All rights reserved.

such as quartz, electricity is coupled to mechanics on account of the polarization of each crystallographic unit cell via strain. Figure 1.3 depicts the effect for one unit cell of quartz in compressive (*left*) and tensile (*right*) deformation along the electrical X_1 -axis, respectively. Compression “squeezes” the unit cell in one distinct direction by displacement of atoms and leads to a polarization of the cell as well as a charging of the respective surfaces (*left*). Since the effect is linear, “elongation” of the cell along the X_1 -axis (*right*) leads to a reverse polarization. As indicated before for one crystallographic unit cell, the charges on the materials’ surface appear due an internal electric field in the crystal. However, the conduction electrons in a metal screen electric fields and prevent bulk polarization. Thus, piezoelectricity is expected to emerge uniquely in insulators. This fact contradicts the proposition of this thesis, that from a phenomenological point of view, nanoporous metal-hybrid materials are expected to behave quite analogously to a piezoelectric solid, even though the underlying mechanism is quite different. Compared to piezoceramics nanoporous metal-electrolyte hybrid materials are novel and thus have a large development potential. For example, mainly noble nanoporous metals, such as platinum [14] or palladium [31] (and of course gold, [8, 32–34]) have been synthesized and investigated so far. Yet, there are experiments on the synthesis of more affordable materials, such as nanoporous copper-nickel [35] or titanium-based alloys [36].

Via the investigation of nanoporous gold as a model material valuable insight into the

mechanisms of electromechanical coupling and deformation behavior at small scale is gained. Specifically, nanoporous metals would be future candidates for a novel type of active strain sensor. Owing to their very large internal surface area and to the large capacitance of electrode surfaces, such strain sensors would be able to create particularly robust electric signals.

1.2 Research aims and experimental approaches

In this work the concept of electromechanical coupling is explored in experiments on nanoporous gold specimens immersed in electrolyte.

The first aim is a proof-of-principle of active strain sensing with nanoporous gold and the quantification of sensing experiments via determining the effective potential-strain coupling parameter ς^* . Secondly, a thermodynamic description of the underlying phenomena that link the novel sensing effect to established observations on actuation has to be derived theoretically and to be verified by experiments. Since the properties of nanoporous gold are tunable, the influence of structure characteristics such as ligament size might play an important role in sensing efficiency and will thus be investigated.

As an experimental approach to obtain meaningful results the measurement strategy exploited on planar gold electrodes had to be implemented in a setup for volumetric samples. Therefore, a dynamic mechanical analyzer was equipped with an electrochemical cell for *in situ* experiments and the electronics, e.g. a Lock-In amplifier, were implemented respectively [5].

1.3 Outline of thesis

The thesis is organized as follows:

Chapter 2 gives the theoretical background for interpretation and discussion of the results obtained in this work. It introduces nanoporous gold and provides basic aspects of metal-electrolyte interfaces and the processes that determine the characteristics of such interface. The electromechanical coupling, the mechanism which governs the sensing behavior of nanoporous gold is introduced via fundamental thermodynamics, followed by the example of a planar electrode, and resulting in a description of microscopic and macroscopic stress in a nanoporous gold network. Subsequently the measurement techniques exploited in this work are presented.

Chapter 3 describes the synthesis of nanoporous gold samples. Additionally a description of the experimental procedures and measurement techniques employed in this work is given.

In **Chapter 4** the results of actuation and active strain-sensing on nanoporous gold are presented. It starts out with the actuation measurements and gives a detailed compendium over the performed strain-sensing experiments. The sensing Section begins out with showing the proof-of-principle, then going further into detail via determining the effective potential-strain coupling parameter, ς^* , of the investigated nanoporous gold specimen. This parameter quantifies the electromechanical coupling and thus, the sensing efficiency of the sensor. The later Sections deal with the dependence of the electromechanical coupling on frequency and structural properties such as connectivity and surface area.

Chapter 5 provides the discussion of the results in a more general context and gives a classification of the sensing efficiency of nanoporous gold via theoretical predictions and comparison to high-performance piezoceramics.

Chapter 6 summarizes the results of this work and gives a short outlook, pointing towards future applications of nanoporous metals in sensing devices.

2 Theory

2.1 Fundamentals of electrochemistry

This Section deals with the fundamentals of electrochemistry that are exploited throughout this work. Starting with very basic concepts, more evolved procedures and approaches will be discussed in the following Sections.

2.1.1 Electrochemical cell

In general, the investigated electrochemical systems consist of at least two electronic conductors (*electrodes*) and one ionic conductor (*electrolyte*). These so-called *electrochemical cells* contain collections of interfaces that separate the different phases. The system can be characterized by the potential difference measured between the electrodes. This potential takes differences in electric potential between the electrodes and the electrolyte in the cell into account.

2.1.2 The ideal polarized electrode and electrical double layer

An *ideal polarized* electrode (IPE) is an electrode which metal-solution interface behaves ideally analogous to a capacitor, i.e. only capacitive processes take place. A capacitor can be described via

$$\frac{q}{E} = C \quad , \quad (2.1)$$

where q denotes the charge stored on the capacitor, E the potential across the capacitor, and C the capacitance. Due to an applied potential E charge is accumulated on the metal plates of the capacitor until equation (2.1) is fulfilled. A current flows during this charging process. The charges on a metal electrode Q^M and in solution Q^S exist at a given potential, with $Q^M = -Q^S$ at all times. Figure 2.1 depicts how the charges are distributed at a metal-electrolyte interface. Q^M is allocated in a very thin layer (< 0.01 nm) on the metal surface, whereas Q^S consists of excess cations or anions in vicinity of the metal surface. The whole array of charges at the metal-electrolyte interface is called the *electrical double layer*.

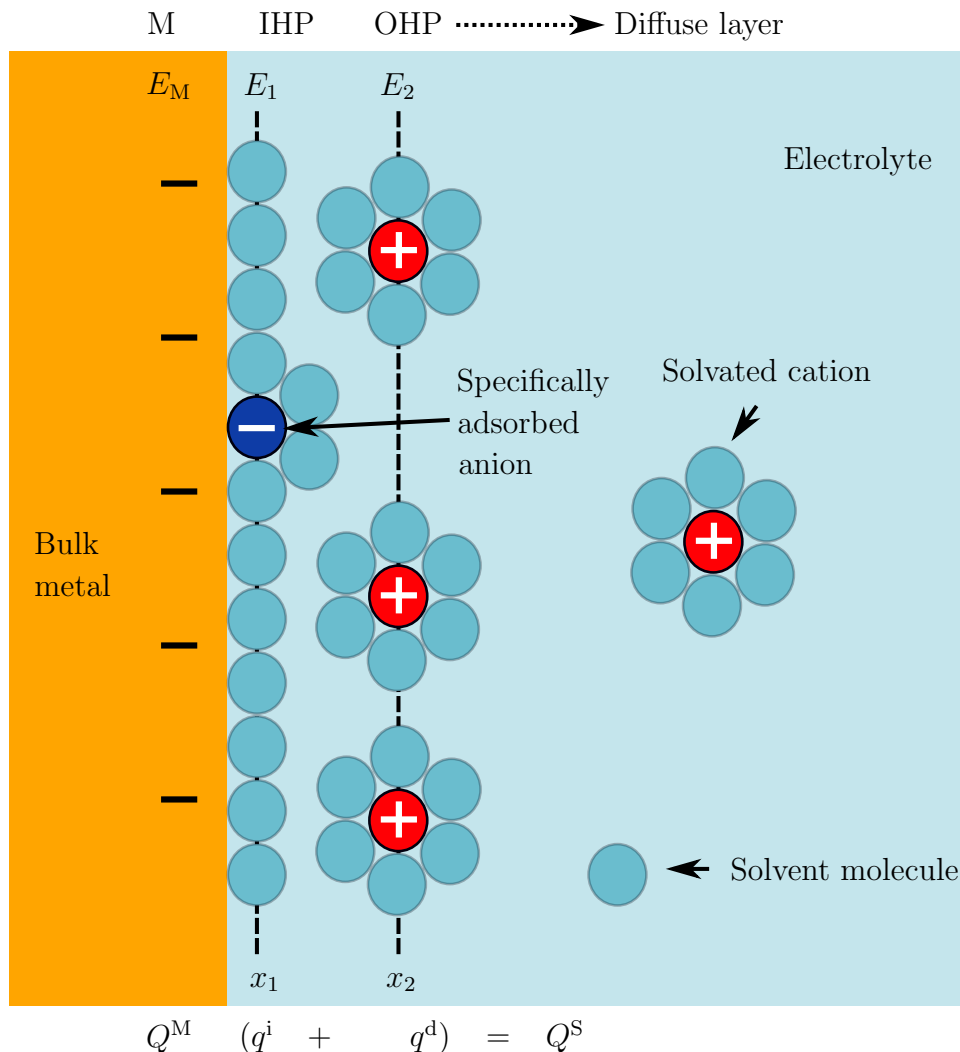


Figure 2.1: Schematic of electrical doublelayer under conditions where anions are specifically adsorbed, adapted from Bard *et al.* [37]. A metal electrode M is immersed in electrolyte. E_M , E_1 , and E_2 denote metal, inner Helmholtz plane (IHP), and outer Helmholtz plane (OHP) potentials, respectively. The excess charge of the IHP, q^i , and of the diffuse layer, q^d , add up to the solution charge Q^S , which is $-Q^M$ (excess charge of metal electrode).

As indicated in Fig. 2.1, the Helmholtz plane consists of the *inner Helmholtz plane* (IHP) and the *outer Helmholtz plane* (OHP). The IHP contains ions or molecules that are specifically adsorbed, i.e. the electrical centers are at a distance x_1 from the metal surface, whereas the OHP contains solvated ions of which the electrical centers of the closest ions are located at a distance x_2 from the metal surface. The OHP is extended to the bulk solution by the so-called *diffuse layer* due to thermal agitation of the solution. The total charge of the solution is given via $q^i + q^d = Q^S$, where q^i and q^d are the excess charges of the IHP and the diffuse layer, respectively. The total ionic concentration in the solution

influences the thickness of the diffuse layer, which is less than ≈ 10 nm for concentrations greater than 10^{-2} M [37].

2.1.3 Faradaic and capacitive processes

Variations of the superficial charge density, i.e. charge per surface area of the electrode A , include capacitive or pseudo-capacitive processes. In capacitive processes charge is stored via ion accumulation in the diffuse layer, whereas in pseudo-capacitive processes charge is stored via ion accumulation in the inner Helmholtz layer. The superficial charge density, q^A , is linked to the superficial excess, Γ_i , via [38]

$$0 = q^A + z_i F \Gamma_i \quad , \quad (2.2)$$

where z_i denotes the valency of the ions in solution and F denotes the Faraday constant. The superficial excess Γ_i includes excess species located in the inner and outer Helmholtz layer and its definition does not distinguish between both. When an ion (e.g. a proton) is specifically adsorbed, a charge transfer between electrode and adsorbed ion converts the adsorbate effectively into a neutral atom. This local process does not change the net charge on the electrode, hence the adsorbed atom still takes part in Γ_i and, therefore, in q^A . When the adsorbed atom is desorbed (e.g. in a cyclic process), the proton goes in solution and is restored with the extra electron in the metal surface. On that note the charge stored via the adsorbate is recoverable, although specific adsorption/desorption typically is not reversible in a thermodynamic sense. The pseudo-capacitive current density, j_{pc} , which is given by the expression [38]

$$j_{pc} = \frac{dq^A}{dt} \quad , \quad (2.3)$$

includes the above mentioned pseudo-capacitive processes, as well as purely capacitive processes.

The Faraday current density, j_F , corresponds to interfacial reactions. It is connected to the not-recoverable transfer of charge and thus, it is unrelated to q^A . Specifically, j_F is assumed to be specified by the electrode potential, E . The net current, j , (i.e. the sum of the pseudo-capacitive variations of the interfacial charge density q^A as well as the reaction current) is then given via [38]

$$j = \frac{dq^A}{dt} + j_F(E) \quad . \quad (2.4)$$

2.2 Electromechanical coupling

This Section deals with the theory of electrochemical actuation and sensing with nanoporous solids.

2.2.1 Thermodynamics of electrodes

A thermodynamic description of the interface of an electrode in contact with electrolyte regarding mechanics and electrochemical phenomena is given following the chapter “Electrocapillarity of Solids and its Impact on Heterogeneous Catalysis” in the book “Electrocatalysis; Theoretical Foundations and Model Experiments, Volume 14” [38], and the study “Balance of Force at Curved Solid Metal-Liquid Electrolyte Interfaces” by Weissmüller and Kramer [2].

Here, a polarizable metal-electrode (**B**) immersed in a fluid electrolyte (**F**) is considered. The solid electrode is an elastic material that transfers charge via electronic transport; no exchange of matter with the electrolyte occurs and only isothermal processes are considered. The thermodynamic potential of choice is the free energy \mathfrak{F} , since the temperature, T , is held constant. The net free energy, \mathfrak{F} , is composed of the contributions from the bulk phases, **B** and **F**, and the interfacial contribution, **S**:

$$\mathfrak{F} = \mathfrak{F}^{\text{B}} + \mathfrak{F}^{\text{F}} + \mathfrak{F}^{\text{S}} \quad (2.5)$$

The free energy densities (per corresponding volume V) Ψ^{B} and Ψ^{F} represent the energetics of electrode and the electrolyte, respectively. The superficial free energy density, ψ (per area A of the electrode surface) expresses the corresponding contribution of the electrode-electrolyte interface. The total net free energy from Eq. (2.5) emerges as [39]

$$\mathfrak{F} = \int_{\text{B}} \Psi^{\text{B}} dV_{\text{B}} + \int_{\text{F}} \Psi^{\text{F}} dV_{\text{F}} + \int_{\text{S}} \psi dA \quad (2.6)$$

where V_{B} and V_{F} denote the volume of the bulk electrode and liquid, respectively. Throughout this work the volume V and area A are stated in Lagrangian coordinates, i.e. V and A are investigated in a strain-free reference state. Thus, in purely elastic deformation A does not change. The densities, such as ψ , for any configuration of the surface are defined as the energy of the actual state, per area of the surface in its undeformed state.

The free energy density function of the electrode is constitutively assumed as $\Psi^{\text{B}} = \Psi^{\text{B}}(T, \mathbf{E})$, and the free energy density of the electrolyte is constitutively assumed as $\Psi^{\text{F}} = \Psi^{\text{F}}(T, \rho_i)$, where \mathbf{E} denotes the strain tensor and ρ_i the densities of the components i in the electrolyte. As stated before, only isothermal processes are discussed here,

therefore T will not be displayed in the following. The fundamental equation of the bulk electrode Ψ^B is then given via $d\Psi^B = \mathbf{S}d\mathbf{E}$ and the fundamental equation of the bulk electrolyte is $d\Psi^F = \mu_i d\rho_i$, where \mathbf{S} is the stress tensor and μ_i is the chemical potential of component i .

To analyze the interface of the system appropriate state variables have to be identified. In a general approach the superficial free energy density ψ depends on the state of the bulk phases in contact, i.e. their state variables, the strain in the solid phase, \mathbf{E} , and the densities in the fluid phase, ρ_i .

Considering a surface with a sufficiently high symmetry the capillary forces in the plane are isotropic [40]. This assumption is only valid for isotropic surfaces and one has to define an arbitrary referential state, e.g. where $e = 0$. Under these assumptions e , defined via $\delta e = \delta\hat{A}/\hat{A}$, is a suitable state variable concerning strain. $\delta\hat{A}/\hat{A}$ denotes the relative change in physical area during the deformation.

It can be shown for fluids far from a critical point that $\partial\psi/\partial\rho_i = 0$. Thus, the surface free energy \mathfrak{F}^S cannot explicitly depend on the composition of the fluid.

The surface free energy density ψ depends on Γ_i , which is the superficial excess per area measured of species i including adsorbed atoms (ions) as well as extra ions in the diffuse layer. Via Eq. (2.2) Γ_i and the charge density q^A are related everywhere on the interface. A general constitutive equation for the surface is now formulated as $\psi = \hat{\psi}(\Gamma_i, e)$, following the above stated assumptions. Furthermore, it is assumed that no exchange of matter with the bulk is possible and that the chemical potentials μ_i are constant for every state of strain. Under these assumptions Γ_i and q^A are monotonic functions of the electrode potential E . Thus, E can be taken as the state variable, instead of considering the Γ_i for each species i separately. The energy-conjugate variable to E is q^A , which leads to $\hat{\psi}(\Gamma_i, e) = \psi(q^A, e)$. The fundamental equation is then derived as follows

$$d\psi = Edq^A + fde \quad (2.7)$$

where the energy-conjugate variable to e is the scalar surface stress $f = \frac{1}{2}\text{tr}\mathbf{S}$ [2].

2.2.2 Electromechanical coupling parameter

The surface stress at a clean surface is not negligible. As indicated in Fig. 2.2 a) truncating a bulk crystal creates dangling bonds at the newly formed surface (shown in Fig. 2.2 b)). These bonds relax and form strengthened bonds in the plane of the surface. Due to this strengthened bonding, a closer interatomic spacing in the surface plane compared to the bulk of the underlying crystal is favored. The arising stress induced by the bulk lattice preventing a closer lattice spacing is identified with the surface stress (see Fig. 2.2 c)).

This microscopic behavior exhibits the general trend of positive surface stress of metals, i.e. the underlying lattice is compressed tangentially [38].

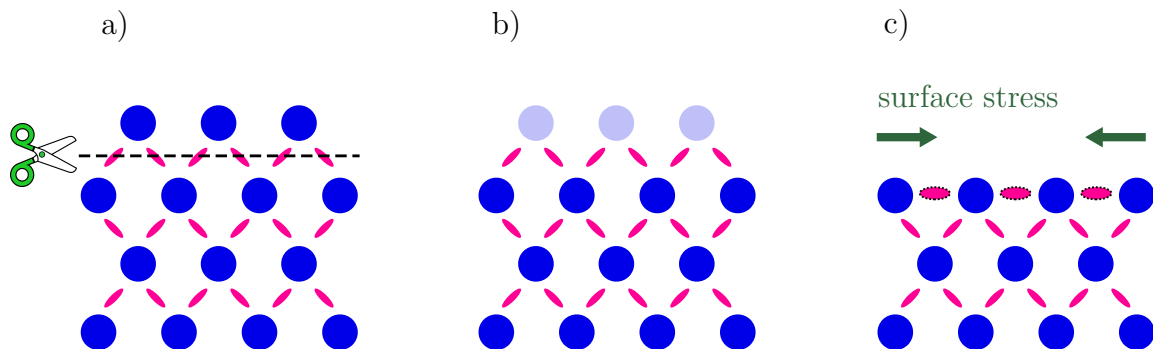


Figure 2.2: Schematic of the microscopic origin of surface stress. a) Cross section of bulk crystal, blue circles depict atoms and pink ovals depict interatomic bonds. If the crystal is truncated as indicated by the dashed black line a new surface will be created. b) shows the unrelaxed and as-truncated surface exhibiting dangling bonds. These bonds will relax and form new bonds, as indicated in c). The new-build bonds correspond to the bonds in surface plane that strengthen the in-plane bonding. Therefore, interatomic spacing of the surface atoms is preferably decreased compared to the bulk. This leads to stress on the bulk crystal that is induced by the surface atoms. Schematics according to Ref. [38].

To describe the interface thermodynamically the fundamental equation of the superficial free energy density, ψ , with $\mathfrak{F}^S = \int_S \psi dA$ was defined in the previous Section 2.2.1.

The second derivative of ψ , given via

$$\varsigma = dE/de|_{q^A} \quad (2.8)$$

represents a fundamental materials parameter of the electrode surface. The electrocapillary coupling parameter ς expresses the coupling between potential and strain. Via the following Maxwell equation

$$\left. \frac{dE}{de} \right|_{q^A} = \left. \frac{df}{dq^A} \right|_e \quad (2.9)$$

one can identify ς also as the surface stress-charge coefficient, that expresses the mechanical response to changes of the superficial charge density [1,2,4]. The surface-stress charge coefficient is accessible via measurements and *ab initio* calculations and has been evaluated as approximately -2V for planar (111)-oriented Au electrodes [5,6].

Although simulation and experimental data agree well for Au, the microscopic origin of the surface-stress charge response is not quite understood yet. The different coupling coefficients ς of different metals have not been related to attributes of excess charge density distributions and charge-induced relaxation. Michl *et al.* in Ref. [41] focused on Al, Mg, and Na that exhibit simple, sp-bonded surfaces and investigated the electrocapillary coupling via *ab initio* simulations. The key finding of these studies is that a generalization

of the interaction of an electric field with the electronic structure of the metal via simple models is elusive.

2.2.3 Nanoporous metal networks as electrodes and their electromechanical coupling

In an interconnected network of nanoscale objects, such as nanoporous gold (np-Au), the stress and strain contributions are more complex than in a planar electrode. A scanning electron microscope micrograph of the structure is shown in Fig. 2.3 a). Here, the charge-induced change in surface stress changes the compensating bulk stresses. The average of the stresses depends on the geometry of the microstructure via the orientation distribution of the surfaces [21]. The modification of the bulk stress leads to a strain throughout the bulk. By projecting the resulting local strains onto the direction of the load-bearing paths in the network an effective macroscopic linear strain, ε^* , (relative change in sample length) is obtained. The effective strain emerges as [39]

$$\delta\varepsilon^* = -\frac{2\alpha\Theta}{9K}\delta f \quad , \quad (2.10)$$

where K denotes the bulk modulus of the solid phase, α the specific surface area ($\alpha = S/V_{\text{solid}}$), and Θ a dimensionless parameter that depends on Poisson's ratio, ν , and on the microstructure of the solid.¹

As indicated in Figures 2.3 a) and b) the np-Au network can be approximated as an idealized geometry where the ligaments are represented by cylindrical wires. For this simplified microstructure $\Theta = \frac{3}{2}(1 - \nu)/(1 - 2\nu)$ or ≈ 7.0 is found (for gold, $\nu = 0.44$), whereas Θ is found to be 5.5 from a molecular dynamics simulation with more realistic geometry for np-Au [39].

The thermodynamic Maxwell relation (2.9) relates the charge-response of f to the response of the electrode potential, E , to tangential strain for a planar electrode. The consequences for the idealized np-Au geometry are shown in Fig. 2.3 c) and d). c) depicts the actuation scenario: Charging the surface leads to expansion or contraction of the ligaments in np-Au. The reverse case is shown in d): straining of the ligament leads to accumulation of charge (at constant potential) or to potential variation (at open circuit and constant charge).

¹Equation (2.10) is derived via continuum mechanics. No general relation between the mean stress and the macroscopic dimensional change could be identified, although one can tailor the relation via Θ . By Weißmüller *et al.* in Ref. [39] an array of cylindrical voids, of spherical voids, a granular solid, and a network of fibers have been discussed and Θ has been evaluated for such structures.

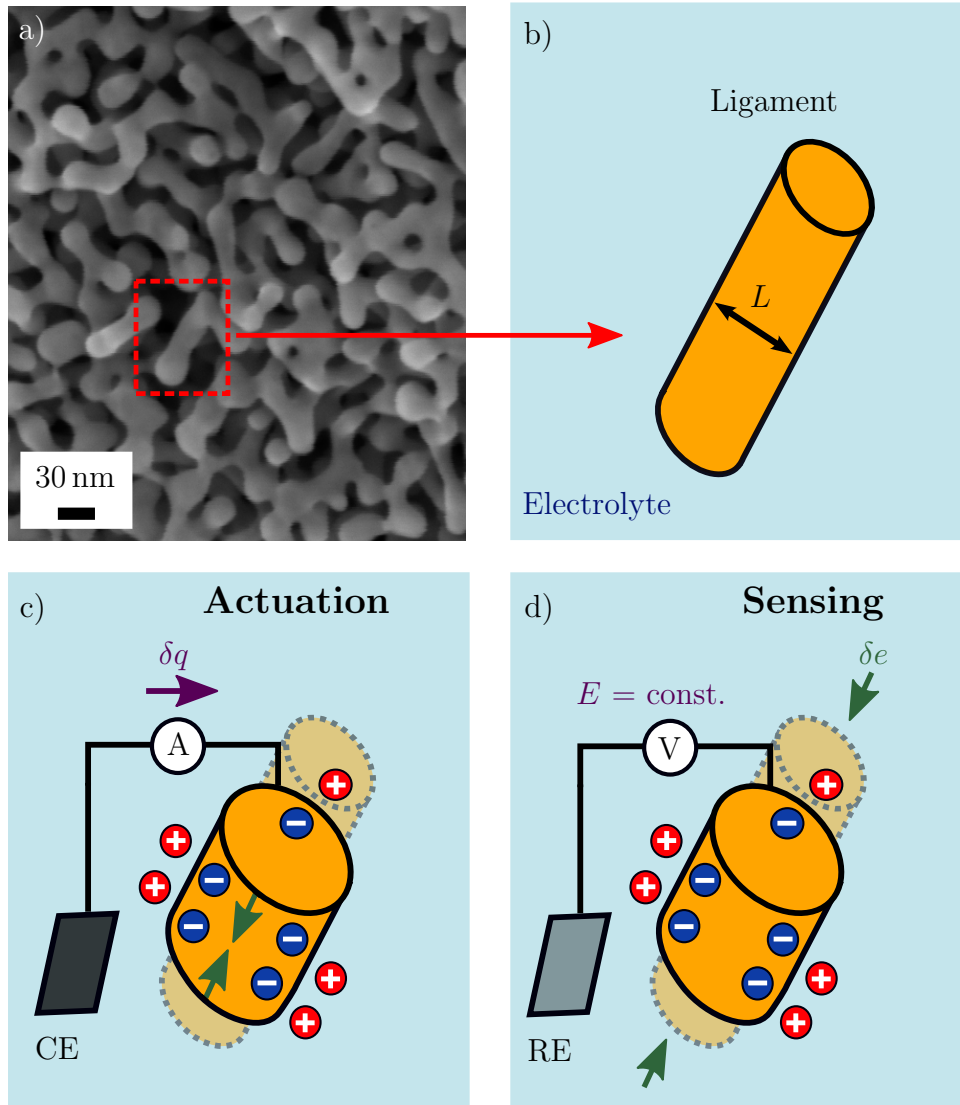


Figure 2.3: Schematic of sensing and actuation mechanism of a nanoporous hybrid-material. a) Scanning electron micrograph of nanoporous gold (np-Au) fraction surface. Red box indicates the resemblance of a single ligament with a cylindrically shaped wire shown in b). b)-d) Schematic illustrations of single ligament immersed in electrolyte. b) shows a circular wire that represents a ligament of size L . In c) the actuation mechanism is depicted: By imposing a charge, δq , a contraction (green arrows) of the wire is induced. The strain acting on the ligament is indicated by green arrows. Charge flows between the counter electrode (CE) and the wire. d) shows the sensing mechanism: By imposing an axial strain, δe , a spontaneous accumulation of electric charge at the wire surface is observed, if a constant potential is applied. Green arrows indicate strain and the potential is controlled between reference electrode (RE) and ligament. Schematics adapted from Stenner *et al.*, see Ref. [42]. The different electrodes, RE and CE, will be introduced in the following Chapter.

The effect depicted in d) has been predicted [2], but not experimentally demonstrated on np-Au so far (first publication see Stenner *et al.*, Ref. [42]). The microscopic picture introduced in this work does not allow a precise prediction of the potential- or charge response to strain at the macroscopic level.

This is due to the non-uniformity of e in the solid network: A macroscopic deformation of the structure results in a heterogeneous local strain field, therefore e differs from the macroscopic strain. The macroscopic approach that points towards a solution for the problem is part of the results of this work will be discussed in the following Chapters.

3 Experimental

3.1 Nanoporous gold

Nanoporous metals can be synthesized from a master alloy via *dealloying*. Dealloying signifies selective dissolution of one or more components out of an alloy. The constituents that are not dissolved form a sponge-like structure that is characterized by open porosity with a distinct ligament size [43].

In this work the material of interest is nanoporous gold, prepared via electrochemical corrosion from a silver-gold master alloy. The as-prepared structure size is typically in the order of ≈ 5 nm [11]. The internal structure size can be tuned via coarsening of the ligaments e.g. by thermal or electrochemical annealing of the sample [44,45].

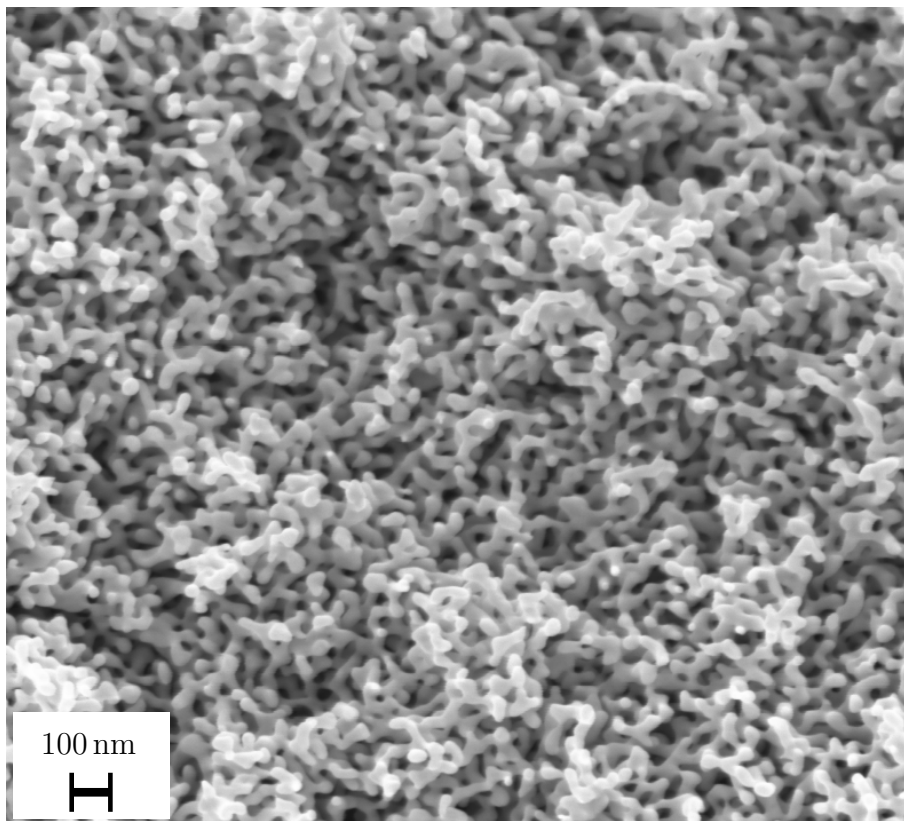


Figure 3.1: Scanning electron micrograph of fraction surface of nanoporous gold specimen. The micrograph shows the interconnected network of ligaments with a size of 40 nm.

Figure 3.1 shows a scanning electron micrograph of a specimen prepared from an $\text{Au}_{25}\text{Ag}_{75}$ master alloy, i.e. the alloy is composed of 25 at.% gold and 75 at.% silver. Due to electrochemical annealing the ligament size is found to be 40 nm. For convenience of sample handling in the performed experiments the macroscopic specimen has a size of a few millimeters. The solid fraction, φ , of the sample has been determined as 0.26. The effective Young's modulus of such samples has been found to be approximately 900 MPa. The techniques of sample characterization will be introduced in the following Section.

One widely discussed concept, the Gibson-Ashby scaling relation, involves the Young's modulus, Y^* , of the solid phase and the solid fraction, φ , to predict the effective Young's modulus of a porous solid [46]. However, nanoporous gold exhibits a much lesser Y^* than theoretically expected based on the scaling relation. An explanation of this deviation, which is suggested by literature (see Refs. [10, 47]), involves the concept of disconnected ligaments or so-called dangling ligaments: Some ligaments are disjointed and therefore they are not participating in the deformation of the load-bearing backbone of the structure. Thus, these dangling ligaments have no influence on strength or stiffness of the macroscopic material. By removing these broken ligaments one would obtain a "mechanically equivalent" network consisting only of load-bearing ligaments. The structure would exhibit a strength and stiffness identical to that of the initial structure. A possible approach to synthesize such structures is to dealloy from master alloys with a higher gold fraction [48], than the commonly exploited $\text{Au}_{25}\text{Ag}_{75}$ alloy, e.g. $\text{Au}_{30}\text{Ag}_{70}$, which is used in this work.

However, the most characteristic feature of nanoporous gold is not the overestimated stiffness by Gibson-Ashby, but the very high surface area-to-volume ratio. Due to this feature the properties of nanoporous metals are mainly determined by their interface [14]. By impregnating the nanoporous metal with electrolyte, one obtains a huge metal-liquid interface that can be accessed electrochemically. This new class of materials opens up further possibilities for exploiting the structural features of nanoporous gold, as will be discussed in the following.

3.2 Measurement techniques

In this Section the employed measurement techniques and corresponding devices will be introduced and discussed.

3.2.1 Three electrode setup

In a *three electrode setup* the current I is flows between the working electrode (WE) and a counter electrode (CE). The electrochemical properties of the CE should not affect the

behavior of the WE. Therefore, the material of the CE is typically chosen as a material that does not produce substances by electrolysis that could reach the WE surface and cause reactions there. The WE potential E is controlled relative to a separate reference electrode (RE), positioned with its tip nearby. A schematic of the arrangement is depicted in Fig. 3.2.

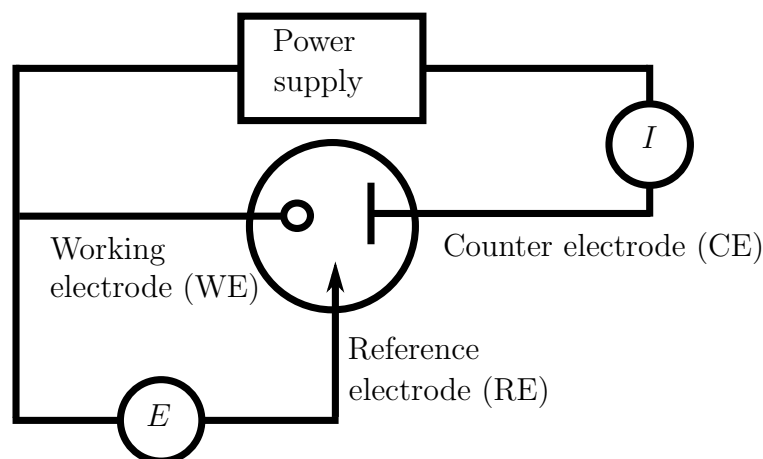


Figure 3.2: Schematic of three electrode setup used in experiments throughout this work. The current I is monitored between counter (CE) and working electrode (WE), whereas the potential E is measured between reference electrode (RE) and WE. The power supply, usually a *potentiostat*, has a high input impedance to inhibit current flowing between WE and RE. Schematics adapted from [37].

Due to the high input impedance of the device (potentiostat) used to determine and control the potential difference between WE and RE a negligible current flows through the RE [37]. This three-electrode arrangement is used in all electrochemical setups throughout this work.

3.2.2 Reference electrodes

To standardize the reactions taking place in an electrochemical cell the reference electrode (RE) has to have a fixed composition leading to a constant RE potential. Only under this condition the working electrode (WE) is accountable for any changes in the cell. Since the potential of the WE is controlled with respect to the RE, the potential of the RE has to be quantified. The internationally accepted primary reference is the standard hydrogen electrode (SHE), which potential is defined via the reduction of protons at a platinum electrode, $2\text{H}^+ + 2e^- \rightarrow \text{H}_2$. This reaction indicates the current standard for zero potential, i.e. $E_{\text{SHE}} = 0$. All other commonly used REs have an offset with respect to SHE, which can be determined via measuring the potential difference (ΔE) between RE and a standardized reference with an known potential vs SHE [37].

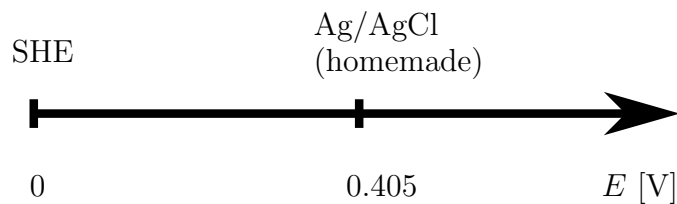


Figure 3.3: Offset of quasi reference electrode (Ag/AgCl) compared to a standard hydrogen electrode (SHE) in 0.5 M H_2SO_4 .

The reference electrode used throughout this work is the (homemade) silver silver-chloride Ag/AgCl quasi reference electrode. Its bias vs SHE is indicated in Fig. 3.3 for a solution of 0.5 M H_2SO_4 . In 1 M HClO_4 the offset was determined as 0.510 V. All potentials in this work are specified vs the quasi Ag/AgCl reference electrode if not stated otherwise.

3.2.3 Chronoamperometry

By applying a potential step via an external voltage source a current flow can be induced at the electrode. In *chronoamperometry* experiments this current is recorded as a function of time. Figure 3.4 shows an exemplary measurement of a potential step applied to a

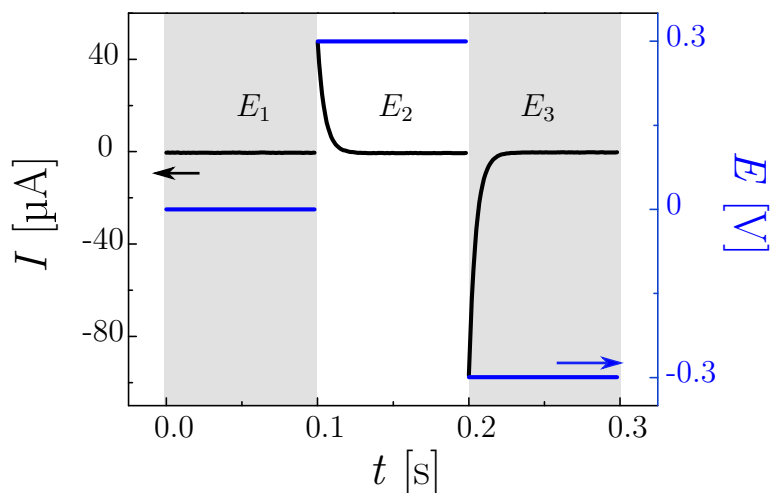


Figure 3.4: Chronoamperometry on a system representing an IPE. The potential is varied in three steps, E_1 , E_2 , and E_3 , indicated by the blue lines. The black lines show the resulting current.

system representing an IPE, i.e. no faradaic currents exists. In the first regime, E_1 , both the potential and current are zero. By increasing the potential to $E_2 > 0$ in one step, the current increases and then decreases exponentially. The same behavior is observed in E_3 , where $E < 0$ and the current flow is therefore of opposite sign. The shape of the curve

is typical for a RC circuit, i.e. a circuit governed by capacitive behavior (here $R = 5 \text{ k}\Omega$ and $C = 1 \text{ }\mu\text{F}$).

3.2.4 Cyclic voltammetry

To characterize the thermodynamic and kinetic properties of electrodes *cyclic voltammetry* is widely applied. It is a consequence of chronoamperometry; the potential is increased or decreased stepwise¹ (or even linearly) whereas the corresponding current I is recorded as a function of the potential E . The results are compiled in a *cyclic voltammogram* (CV). Reaction potentials, e.g. for oxidation or reduction, can be identified in a CV, as well as regions of capacitive charging, i.e. where no reactions take place. The shape of the CV is highly dependent on the scanrate, ν , since it defines the measurement time at each step and therefore the current flow that is measured.

Figure 3.5 shows a CV performed on a nanoporous gold sample immersed in 1 M HClO₄. The potential is swept stepwise to a potential E_2 and then backwards to E_1 at a constant scanrate ν . The triangular shaped potential progression is shown in the inset of Fig. 3.5. The current I induced by the potential sweep on a nanoporous gold electrode is indicated by the dark red line in Fig. 3.5, the arrows show the scanning direction. This cyclic voltammogram is divided in three regimes, I) (blue), II) (yellow), and III)(red). Regime I) is the capacitive or double layer regime, where charge is accumulated or depleted at the electrical double layer. In positive scan direction a peak appears in regime III) at $\approx 1.25 \text{ V}$ indicating anion adsorption (here: OH⁻). The distinctive peaks that correspond to specific surface facets of np-Au and therefore lead to the shape of the adsorption profile have been investigated by Wang, *et al.* in Ref. [50]. For a similarly prepared specimen as shown here, it was found that the highest peak at $\approx 1.26 \text{ V}$ corresponds to the oxidation of {111} facets, whereas the smaller peak $\approx 1.4 \text{ V}$ corresponds to the oxidation of {100} facets and/or step/kink sites.

During the backward scan starting from E_2 a dip at $\approx 1.1 \text{ V}$ at regime II) is observed. It corresponds to desorption of the oxide film. The processes taking place during a CV are highly time dependent, therefore one has to choose a suitable scanrate [37, 50, 51].

¹In *staircase* cyclic voltammetry the current is usually determined at the end of each potential step. Here, the total charge that was measured during each potential step was integrated yielding in a total current per step, i.e. faradaic and capacitive components are taken into account. The staircase cyclic voltammetry technique is employed throughout this thesis, since very small scanrates $\nu = \frac{dE}{dt}$ can be applied [49].

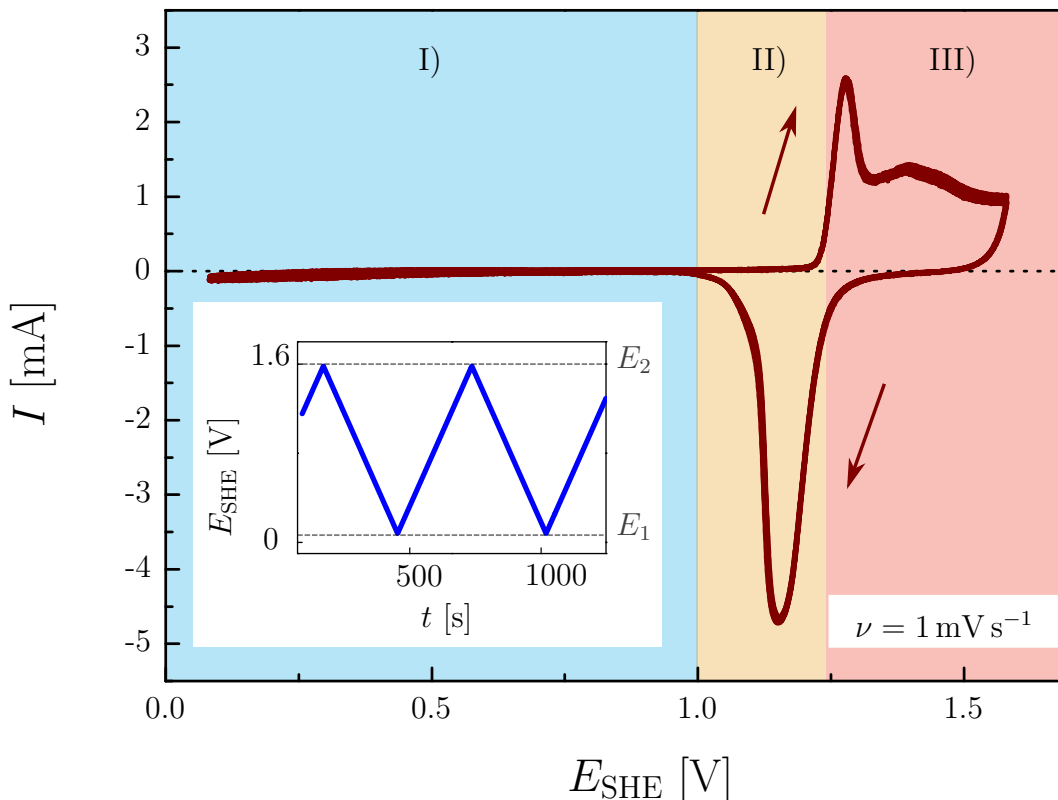


Figure 3.5: Cyclic voltammogram of nanoporous gold specimen in 1 M HClO_4 . Background colors blue, orange, and red indicate the capacitive I), oxygen-desorption II), and oxygen-adsorption regime III), respectively. Scanrate is $\nu = 1 \text{ mV s}^{-1}$ and the red arrows indicate the scanning direction. The inset shows the applied potential versus time (blue line). The potential is measured versus the standard hydrogen reference electrode, as indicated by the subscript E_{SHE} .

3.2.5 Impedance spectroscopy

A frequently used circuit to describe an electrochemical cell for impedance spectroscopy, the *Randles equivalent circuit*, is shown in Figure 3.6.

The parallel elements are introduced because the total current through the electrolyte-metal interface is the sum of distinct contributions from double-layer charging and faradaic process, i.e. $i_C + i_f$. The double-layer capacitance is represented by the pure capacitance, C . The faradaic process is taken into account as a general impedance, Z_f . The faradaic impedance can be considered in various ways, e.g. as a combination of polarization resistance and a pseudocapacitance or a charge-transfer resistance and an impedance representing a resistance to mass transfer. The components of the faradaic impedance are not ideal, because they change with frequency, ω . Since all of the current has to pass through the solution resistance of the electrolyte, R_E , it is inserted as a series element [37]. There are many examples of equivalent circuits for more complex geometries, such as porous materials [52] or metals with organic coatings [53].

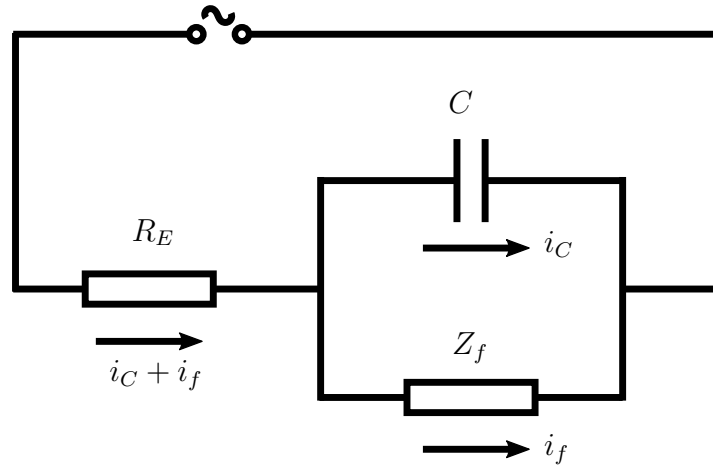


Figure 3.6: *Randles equivalent circuit* of electrochemical cell. The circuit consists of a resistance R_E , representing the ionic resistance of the electrolyte in series with a parallel circuit. The parallel circuit is composed of a capacitance C , representing the capacity of the electrochemical double layer and an impedance Z_f representing the faradaic impedance. A sinusoidal potential is applied to measure the current response composed of faradaic and capacitive currents, i_f and i_C , respectively. Schematics adapted from Ref. [37].

Nevertheless, in the following impedance spectroscopy will be discussed by means of the Randles equivalent circuit: Via applying a sinusoidal potential excitation to an electrochemical cell represented by the circuit shown in Fig. 3.6 one can induce current responses that will be discussed in the following.

As stated before, the capacitance follows equation (2.1). A sinusoidal potential can be expressed as $E = E_0 e^{i\omega t}$, with excitation amplitude E_0 , complex number i , and frequency ω . The current response is analogous with addition of a phase shift. Since $I = \frac{dQ}{dt}$, one can substitute Eq. 2.1 by $I = C \frac{dE}{dt}$. Therefore, the impedance $Z_C = E/I$ is then given via

$$Z_C = \frac{E_0 e^{i\omega t}}{i\omega C E_0 e^{i\omega t}} = \frac{1}{i\omega C} \quad (3.1)$$

This leads to the following expression for the impedance $Z_{Z_f, C \text{ parallel}}$ of the parallel part of the equivalent circuit

$$Z_{Z_f, C \text{ parallel}} = \frac{Z_f}{1 + i\omega Z_f C} \quad (3.2)$$

Thus, impedance of the whole circuit, parallel part plus solution resistance can be calculated as

$$Z = R_E + \frac{Z_f}{1 + i\omega Z_f C} \quad (3.3)$$

This expression can be simplified and written in the form of a complex number ($Z = Z' + iZ''$) as follows

$$Z = R_E + \frac{Z_f}{1 + \omega^2 Z_f^2 C^2} - i \frac{\omega Z_f^2 C}{1 + \omega^2 Z_f^2 C^2} \quad (3.4)$$

Via eliminating ω one can obtain the following relation from Eq. (3.4) between the real and imaginary part of Z [53]:

$$\left[Z' - \left(R_E + \frac{Z_f}{2} \right) \right]^2 + (Z'')^2 = \left(\frac{Z_f}{2} \right)^2 \quad (3.5)$$

In a simplified and special case with very high frequencies, one can consider Z_f as a pure resistance related to the charge transfer, R_{ct} . This assumption leads to the complex-plane plot shown in Fig. 3.7 a).

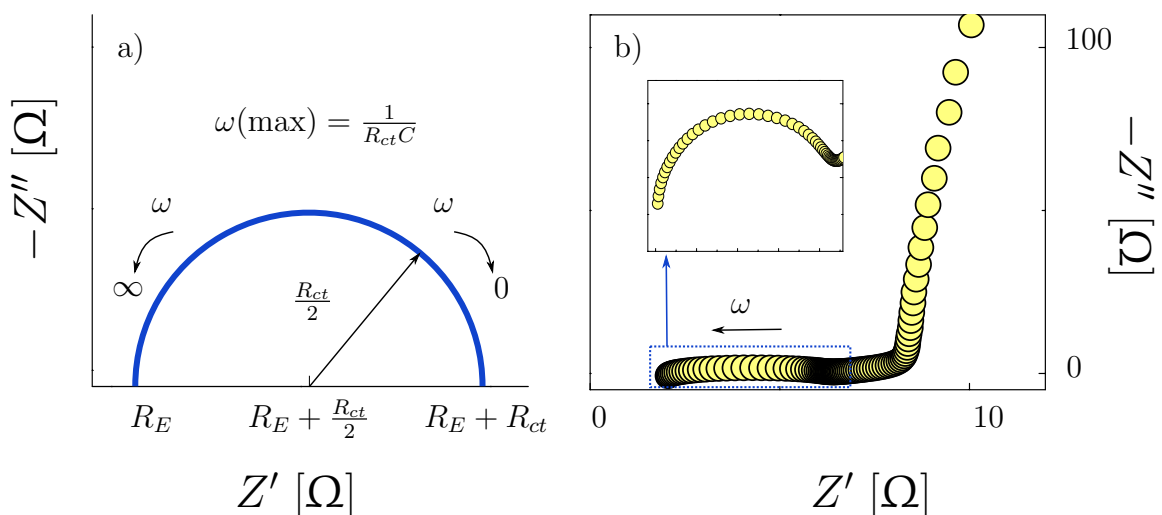


Figure 3.7: Complex-plane plots of equivalent circuit at high frequencies and nanoporous gold. a) Complex-plane plot of equivalent circuit shown in Fig. 3.6 for high frequencies ω . The shape of the curve is a semi-circle, which characteristic properties depend on the solution resistance, R_E , the charge transfer resistance, R_{ct} , and the doublelayer capacitance, C . Adapted from Ref. [53]. b) Impedance data obtained from measurements on nanoporous gold in 1 M HClO_4 at a potential of 0.3 V. The semi-circle at high frequencies is enlarged in the inset.

The diagram shows a semi-circle with radius $R_{ct}/2$, where the imaginary part of the impedance approximates zero for infinite frequency, since Z'' emerges solely from C and its contribution falls to zero at high frequencies (see Eq. (3.1)). All current is charging current, and the only impedance is ohmic resistance. As the frequency decreases, the finite impedance Z_C yields in a maximum of Z'' at $\omega(\text{max}) = 1/(R_{ct}C)$. At very low frequencies, the capacitance C leads to a further increase in impedance Z_C , thus current flows mostly through R_{ct} and R_E . Therefore Z'' decreases. In general, one expects to see a

departure from this plot in the lower frequency regime, since the approximation $Z_f \approx R_{ct}$ is only valid for high frequencies [37]: As indicated in Figure 3.7 b) the behavior of np-Au differs strongly from the before-mentioned special case. The semi-circle is indicated by the inlet and the deviation from the shape of plot a) starts at lower frequencies ($\omega/2\pi \approx 160$ Hz). The linear correlation between Z' and Z'' at lower frequencies point towards a diffusion-controlled electrode process [37]. The phase shift between potential and current is defined as [54]

$$\tan(\phi) = \frac{Z''}{Z'} \quad . \quad (3.6)$$

Considering an ideal polarizable electrode (IPE), the impedance Z_f vanishes and thus, the equivalent circuit is represented by the capacitance C and the solution resistance R_E in series. Hence $Z_{R,C \text{ in series}}$ is governed by the capacitance for small ω and by the resistance for large ω [55], R_E is identified as the real part, Z' , and $(\omega C)^{-1}$ as the imaginary part, Z'' , of the impedance. Considering only low frequencies an effective capacitance of an IPE can be calculated from the applied sinusoidal potential excitation and the resulting current response via $C = I_0/\omega E_0$.

One can also obtain the raw data from impedance measurements, i.e. the applied potential oscillation and the resulting current responses. The traces of these curves are shown in Fig. 3.8.

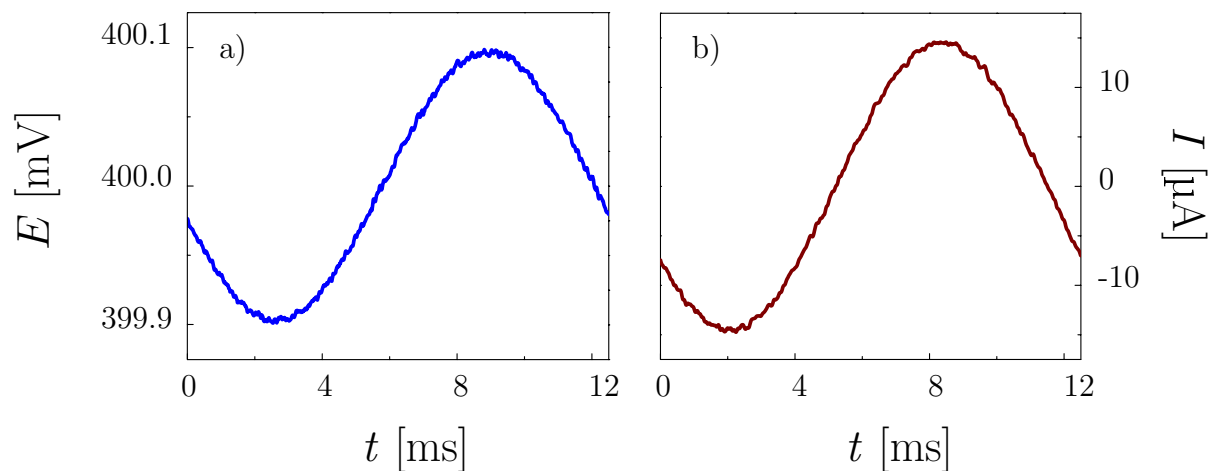


Figure 3.8: Representative potential and current signals obtained via the impedance spectroscopy module. a) A potential modulation with an amplitude of $\hat{E} = 100 \mu\text{V}$ and a bias of 400 mV at a frequency $\omega/2\pi = 76$ Hz is applied to a np-Au sample. The resulting current response is shown in b). The measurement was performed in 0.5 M H_2SO_4 .

Here, a potential oscillation with a frequency of 76 Hz was applied between a np-Au specimen (WE) and a RE. A resulting current oscillation with the same frequency is measured between WE and CE, which corresponds to a purely electrochemical excitation.

3.2.6 Fundamentals of Lock-In amplifiers

Lock-in amplifiers (LIA) are used to detect and measure alternating current (AC) signals even under high noise and high background conditions. Figure 3.9 shows a simplified block diagram of the LIA used in this work.

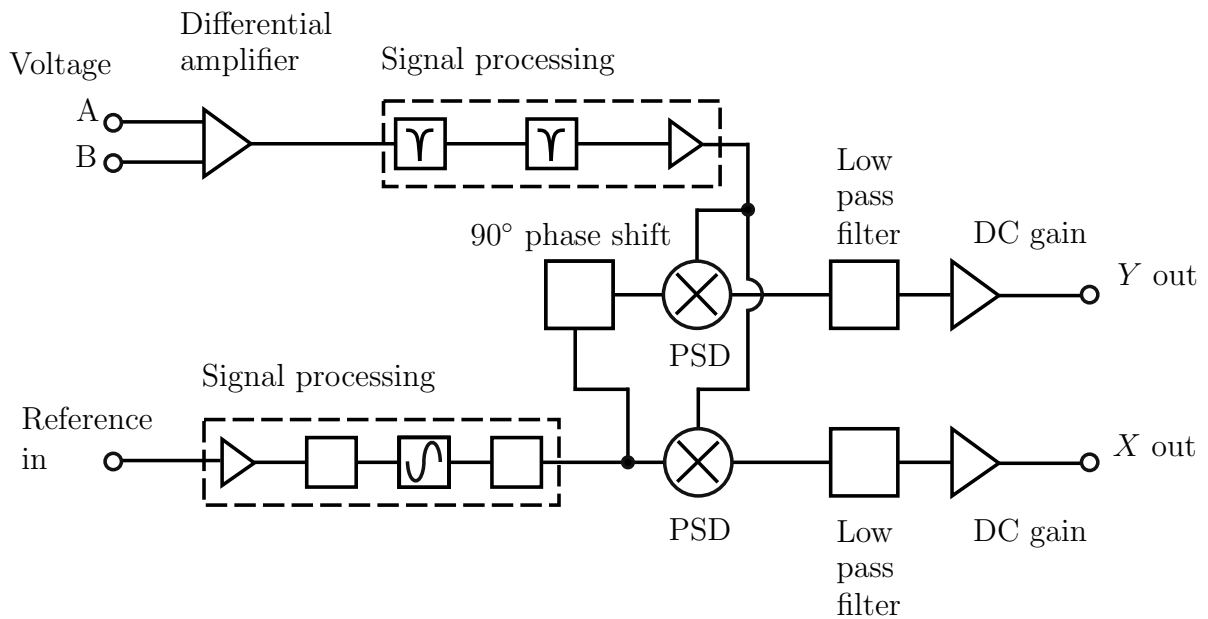


Figure 3.9: Block diagram of Lock-In amplifier (LIA). An AC signal $E(t)$ is applied via the ports “A” and “B” of the LIA and further processed (“Signal processing”). $E(t)$ is then multiplied with a reference signal (“Reference in”, enhanced by “Signal processing”) via a phase-sensitive detector (“PSD”). The resulting signal passes a low pass filter and an amplifier (“DC gain”) before it can be extracted from “X out”. The signal extracted from “Y out” is generated by multiplying the reference signal with a phase shift (“90° phase shift”) before being multiplied (“PSD”) with the processed input signal and passing low pass filter and DC gain. Adapted from Ref. [56].

A sinusoidal voltage, $E(t) = E_A(t) - E_B(t) = E_{\text{sig}} \sin(\omega_{\text{sig}} t)$, is entered into the ports “A” and “B” of the LIA, then the signal is enhanced via a differential amplifier. The signal is processed furthermore (“Signal processing”), e.g. the line frequency and higher harmonics are notched out. To determine phase and amplitude of the resulting signal, a reference signal, $E_{\text{ref}}(t) = E_{\text{ref}} \sin(\omega_{\text{ref}} t + \Theta)$, with a given frequency ω_{ref} and phase shift Θ regarding $E(t)$, has to be exploited from the measurement setup (“Reference in”). The reference signal is further processed through an amplifier and internally stabilized via

the LIA (“Signal processing”) before $E(t)$ and $E_{\text{ref}}(t)$ are multiplied via a phase-sensitive detector or multiplier (“PSD”). The resulting signal can be simplified² as follows:

$$X(t) = \frac{1}{2} E_{\text{sig}} E_{\text{ref}} [\cos([\omega_{\text{sig}} - \omega_{\text{ref}}]t - \Theta) - \cos([\omega_{\text{sig}} + \omega_{\text{ref}}]t + \Theta)] . \quad (3.7)$$

The resulting AC signal, $X(t)$, passes a low pass filter that inhibits all AC components of $X(t)$. However, under the condition $\omega_{\text{sig}} = \omega_{\text{ref}}$ a direct current (DC) signal, X , proportional to amplitude of the measurement signal and cosine of the phase shift is obtained:

$$X = \frac{1}{2} E_{\text{sig}} E_{\text{ref}} \cos \Theta \quad (3.8)$$

X is enhanced via an amplifier (“DC gain”) and can be extracted from the port “X out”. By adding a second PSD with a reference oscillator shifted by 90° (“ 90° phase shift”), i.e. $E_{\text{ref2}}(t) = E_{\text{ref2}} \sin(\omega_{\text{ref2}}t + \Theta + 90^\circ)$, the out-of-phase part of the signal, Y (with $Y \propto E_{\text{sig}} \sin \Theta$), is generated after passing the low pass filter. Y is enhanced via an amplifier (“DC gain”) and can be extracted from the port “Y out”.

Therefore, one can obtain the amplitude of the signal, E_{sig} , as well as in-phase (X , $\cos \Theta$) and the out-of phase (Y , $\sin \Theta$) information. The in-phase part corresponds to the real part of the signal, whereas the out-of-phase part can be identified as the imaginary part. Thus a LIA serves as phase-sensitive measurement device which determines amplitude and phase shift of an AC signal via a reference signal. Furthermore, the LIA has a very high input impedance ($10 \text{ M}\Omega \parallel 2.5 \text{ pF}$) in order to minimize the current drawn from the measurement setup and reduce noise [56].

3.2.7 Dynamic mechanical analysis

Dynamic mechanical analysis is widely used to determine materials’ parameters, such as storage modulus Y' , loss modulus Y'' , and damping factor $\tan(\delta)$. Here we will only inspect compression mode, where a (cylindrically shaped) bulk sample is cyclically compressed in uniaxial direction. The dimensions of the sample are defined as follows: A_S is the cross sectional area and l_0 the sample height, (see Fig. 3.10 a), *above*). In order to obtain material parameters a load consisting of a static and a dynamic component, $F(t) = F_{\text{stat}} + F_{\text{dyn}} \sin(\omega t)$, is applied to the sample via a pushrod, as shown in Fig. 3.10 a), *below*. Simultaneously the dynamic displacement a_{dyn} is measured.

²using the following trigonometric relation: $\sin x \sin y = \frac{1}{2} (\cos(x - y) - \cos(x + y))$

From the raw data and the geometric proportions of the sample one can calculate the stress, $\sigma_{\text{dyn}} = F_{\text{dyn}}/A_S$, and strain, $\varepsilon_{\text{dyn}} = a_{\text{dyn}}/l_0$. Figure 3.10 b) compiles both traces of the stress and strain signals of a representative measurement performed on a nanoporous gold specimen.

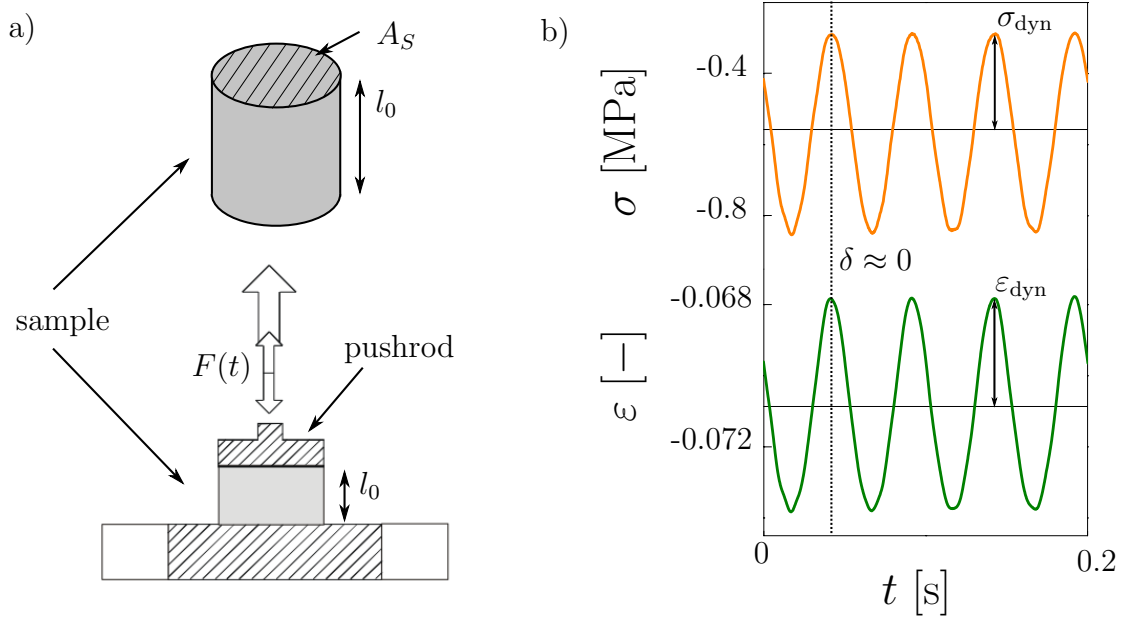


Figure 3.10: Dynamic mechanical analysis setup and representative measurements. a) Schematic of cylindrically shaped sample with cross sectional area, A_S , and height, l_0 , above. Below: Sketch of measurement setup for this geometry adapted from [57]. A dynamic load, $F(t)$, is applied to the sample via a pushrod. b) Representative signals measured on a nanoporous gold specimen via DMA at a frequency $f = 2\pi/\omega = 20$ Hz. The calculated stress, σ , from the applied load is indicated vs. time t (orange line). The green line depicts the induced strain, ε . Stress and strain have dynamic amplitudes of σ_{dyn} and ε_{dyn} , respectively. In this measurement the phase shift between both signals is approximately zero, i.e. $\delta \approx 0$.

As a measure of elasticity the storage modulus Y' in this geometry is ideally equivalent to the Young's modulus, Y . Thus, Y' can be estimated as an “effective Young's modulus” Y^* and is calculated as follows:

$$Y' = \left(\frac{\sigma_{\text{dyn}}}{\varepsilon_{\text{dyn}}} \right) \cos(\delta) \quad , \quad (3.9)$$

where δ denotes the phase shift between applied load and induced strain. The loss modulus Y'' , also called the imaginary modulus, is determined via $Y'' = (\sigma_{\text{dyn}}/\varepsilon_{\text{dyn}}) \sin(\delta)$. From both moduli the damping, which indicates how efficiently the material loses energy to internal friction and molecular arrangements, can be calculated by

$$\tan(\delta) = \frac{Y''}{Y'} \quad . \quad (3.10)$$

Due to its definition $\tan(\delta)$ is independent of geometry effects. The damping is used to determine the phase shift between load and strain and to validate the measurement results [58].

3.3 Sample preparation

3.3.1 Master alloy preparation and dealloying

The precursor (master alloy) ingot composed of 75 at.% silver and 25 at.% gold was alloyed by melting wires (Ag \geq 99.99 %, Au \geq 99.99 %, Sigma-Aldrich) in Ar atmosphere using an arc melter (MAM-1, Edmund Bühler). Another composition synthesized for the experiments was 70 at.% and 30 at.% gold.

The masteralloy-ingot (\approx 2 – 3 g) was sealed in an evacuated (10^{-2} bar) quartz tube and homogenized at 875 – 925 °C for 120 h (furnace RHF1600, Carbolite). The homogenized ingot was then drawn into a wire with (1.3 ± 0.1) mm diameter via a wire-drawing machine. Afterwards, the wire was cut into cylindrically-shaped samples with a length of (2.1 ± 0.1) mm by a diamond wire saw (Model 3032-4, Well) and annealed for 3 h at 650 °C in an evacuated furnace (Mila-5000, Ulvac-Riko) for stress relief.

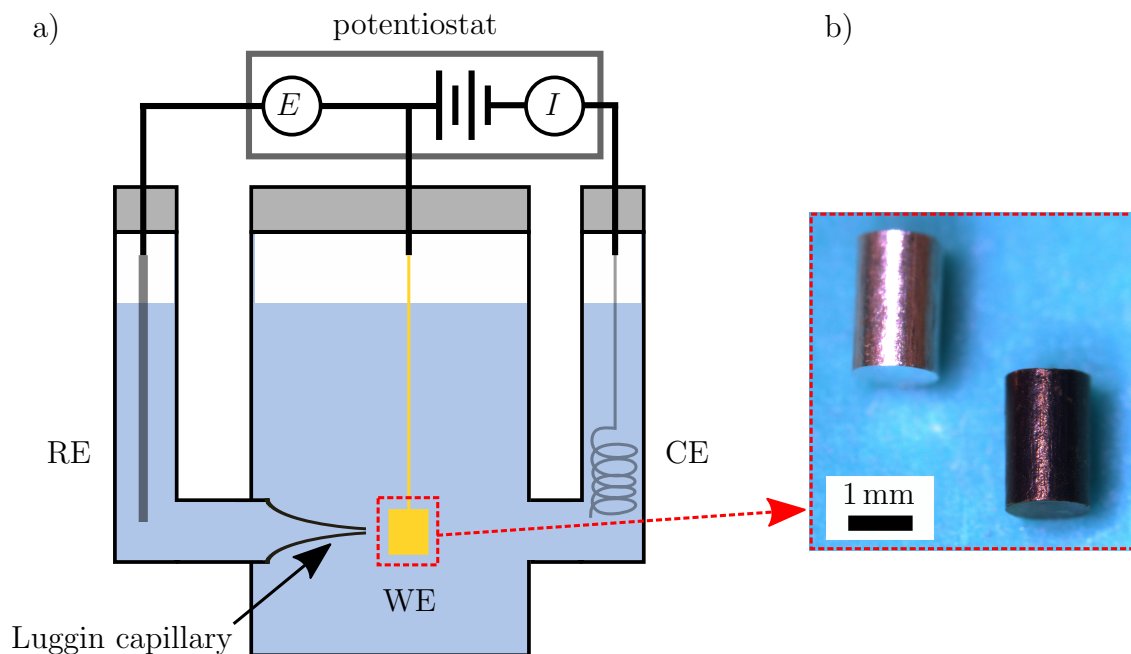


Figure 3.11: Dealloying setup. a) Schematic of electrochemical cell with Ag/AgCl quasi-reference electrode (RE), AuAg specimen in goldbasket as working electrode (WE) and silver wire as counter electrode (CE). The luggin capillary decreases the ohmic drop of potential between working and reference electrode. b) Photograph of AuAg specimen before dealloying (*left*) and nanoporous gold sample after dealloying (*right*).

The cylindrical specimens were dealloyed in a three electrode setup as shown in Fig. 3.11 a). 1 M HClO₄ (Emsure[®], Merck and ultrapure water (18.2 MΩ cm)) served as electrolyte. A homemade silver/silver chloride (Ag/AgCl) electrode was used as reference electrode (RE), the offset of this kind of RE versus a standard hydrogen electrode (SHE) is 0.395 V in 1 M HClO₄. A wound up silver wire served as counter electrode (CE). The working electrode (WE) consisted of up to 6 AuAg specimens in a gold basket. All electrodes were connected to a potentiostat for chronoamperometry. Between WE and RE a potential of 0.75 V vs Ag/AgCl was applied until the current between WE and CE dropped below 10 μA. The Luggin capillary depicted in a) decreases the ohmic drop calculated as IR_E , where I is the current flowing between RE and WE and R_E is the ohmic resistance due to ionic transport in the electrolyte. Since R_E depends on the distance between RE and WE, the tip of the capillary has to be placed very close to the WE [37]. As shown in Fig. 3.11 b) the specimen changes color during this process, from silver shiny (*left*) to black (*right*). After that step a potential of 0.85 V for polarization was applied until the current dropped below 10 μA. In order to dealloy master alloys of a composition of Au₃₀Ag₇₀ the electrolyte was heated in a double-walled cell to a temperature of 50 °C via a thermostat and a potential of 0.78 V vs Ag/AgCl was applied until the current dropped below 10 μA. The polarization potential was 0.83 V and was also applied until the current dropped below 10 mV. Then the cell was cooled down to room temperature. A typical dealloying and polarization process of 6 specimen took 5 days.

3.3.2 Electrochemical and thermal annealing

For the reduction of the oxide layer that was formed during dealloying [34], 20 cyclic voltammograms (CVs) were performed between -0.4 V and 1.1 V at a scanrate ν of 5 mV s⁻¹. This procedure is called *electrochemical annealing*. The oxide layer influences the mechanic properties [59] and inhibits a clean metal surface. For the removal of the oxide layer and for further reduction of the residual silver content the samples were polarized at 0.85 V for 20 min and subsequently 10 CVs with the same parameters as before were performed. The samples were then rinsed with ultrapure water and dried over night. After the electrochemical procedures the samples had a diameter of (1.20 ± 0.05) mm and a length of (2.00 ± 0.05) mm, as measured via an optical microscope. The mean ligament size L of the specimens synthesized from the Au₂₅Ag₇₅ was found as (40 ± 10) nm by scanning electron microscopy and the residual silver content was determined to be below 1 at.% by energy-dispersive X-ray spectroscopy. Calculated from the measured mass and macroscopic volume of the sample the solid volume fraction was $\varphi = \frac{V_{\text{np}}}{V_{\text{cylinder}}} \approx 0.26$, here the volume V_{np} of the nanoporous sample is calculated via $V_{\text{np}} = m_{\text{sample}}/\rho_{\text{Au}}$. The volume of the cylinder is given via $V_{\text{cylinder}} = \pi r^2 l_0$, with r and l_0 radius and length of the

macroscopic cylindrically shaped sample, respectively.

After these procedures some of the specimens were *thermically annealed* under normal atmosphere at 300 °C for 5 min. This leads to an increase in ligament size to $L = (100 \pm 30)$ nm.

The samples synthesized from the $\text{Au}_{30}\text{Ag}_{70}$ master alloy exhibited a ligament size of (30 ± 10) nm, the solid volume fraction was $\varphi \approx 0.3$ and the residual silver content was determined to be approximately 5 at.%

3.4 Measurement setup

As measurement setup served a dynamic mechanical analyzer (DMA; BOSE ElectroForce) with an implemented customized electrochemical cell for *in situ* electrochemical measurements as shown in Fig. 3.12. Figure a) shows an overview of the DMA device, whereas in b) the electrochemical cell is enlarged.

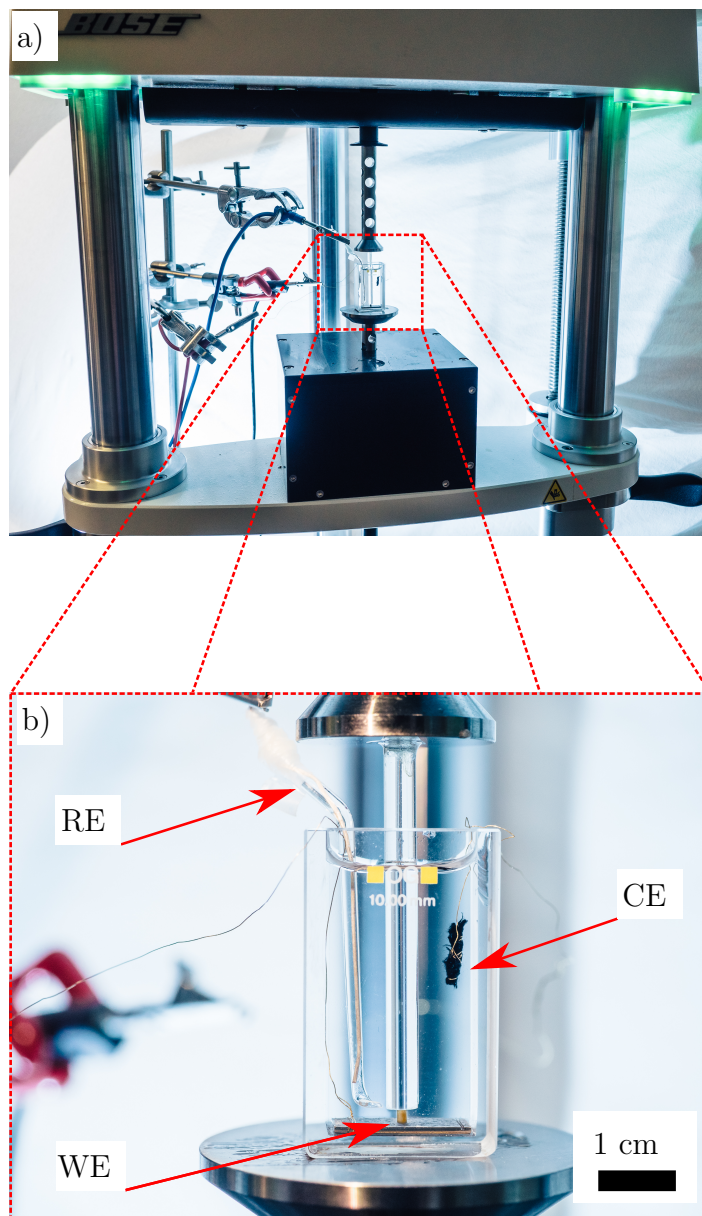


Figure 3.12: Dynamic mechanical analyzer (DMA) setup for *in situ* electrochemical measurements. a) Electrochemical cell mounted in DMA test setup. b) Electrochemical cell for *in situ* measurements. Fused-silica pushrod to apply constant, linear or sinusoidal force. Silver/silver chloride (Ag/AgCl) reference electrode (RE), carbon cloth counter electrode (CE) and nanoporous gold specimen on platinum plate as working electrode.

Actuation and sensing measurements were performed in 0.5 M H_2SO_4 prepared from H_2SO_4 (Suprapur[®], Merck) and ultrapure water (18.2 M Ω cm). Prior to the measurements the solution was deaerated with Argon. Before filling with sulfuric acid the cell was cleaned with Piranha solution³ and rinsed with ultrapure water. In all experiments an Ag/AgCl pseudo-reference electrode, which is + 0.405 V vs. the standard hydrogen electrode (SHE), served as reference electrode (RE). All potentials of this work are specified vs. Ag/AgCl if not stated otherwise. A carbon cloth was used as counter electrode (CE), due to its large surface area (specific surface area 1200 - 1750 m² g⁻¹, Kynol Europa GmbH) and low reactivity. For electric contact the nanoporous gold (np-Au) specimen was placed on a platinum plate connected to the potentiostat (Autolab) via a gold wire. A fused-silica rod was attached to the pushrod of the DMA to transfer the load to the sample, since the stainless steel pushrod of the device is not suitable for electrochemical measurements. Prior to actuation and sensing experiments, all samples were “pre-deformed” *in situ* to a plastic strain ≈ 0.15 at a rate $\dot{\epsilon} = 10^{-4} \text{ s}^{-1}$, see stress-strain diagram (Fig. 3.13). This served to ensure uniform contact at the load surfaces, as indicated by the less pronounced rise in the stress-strain diagram. Furthermore, an increase in effective Young’s modulus with plastic deformation was observed in FEM and MD simulations on np-Au [16, 60]. After pre-deformation the samples were unloaded, as indicated by Fig. 3.13.

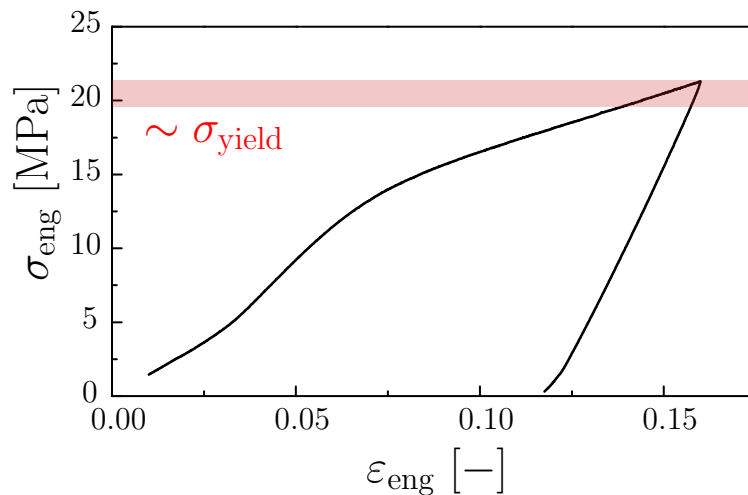


Figure 3.13: Representative stress-strain curve from load-unload experiment of nanoporous gold specimen. Red area indicates the yield stress, σ_{yield} , that can be estimated as ≈ 21 MPa from this measurement.

³Piranha solution was obtained via mixing concentrated sulfuric acid, H_2SO_4 , (Merck, 96%) with hydrogen peroxide, H_2O_2 (Merck, 30%), in a ratio of 8 : 2, respectively. The products are water and H_2SO_5 (Piranha solution), which is strongly acidic, a strong oxidizer and dehydrates organic residues immediately. Therefore, it is widely used in chemistry labs for cleaning glassware and materials that exhibit a high tolerance to acidity.

3.4.1 Determination of surface area

The quasi-static value of the capacity, C of each sample was measured via cyclic voltammetry. To ensure a linear variation of charging current with potential scan rate as in [34] only a small potential window was scanned with different scanrates ν , see Fig. 3.14 a). From Eq. (2.1) one can calculate the dependence of C on current I and scanrate as follows

$$Q = CE \rightarrow I = \frac{dQ}{dt} = C \frac{dE}{dt} = C\nu . \quad (3.11)$$

Note, here $I = I_m$, the mean current flowing for each scandirection. Therefore, the capacity is defined as the slope of I_m vs. ν , as indicated in Fig. 3.14 b). Before and after each experiment, the net surface area, S , in the sample was determined by the capacitance ratio method, $S = C/c$ [61] using the double layer capacitance value of a clean Au surface, $c = 40 \mu\text{F cm}^{-2}$ [62].

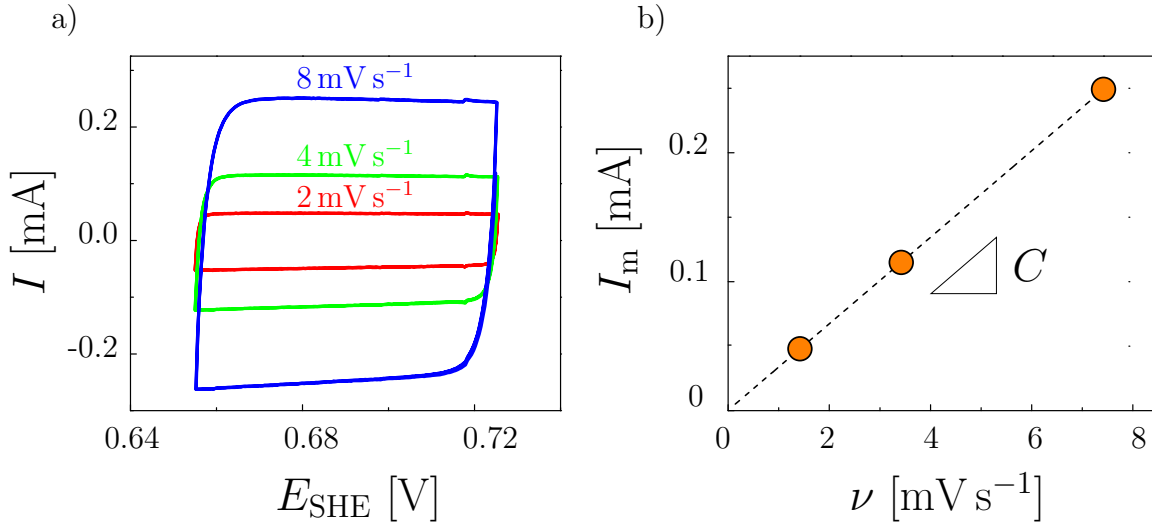


Figure 3.14: Determination of quasi-static capacity. a) Cyclic voltammograms of np-Au specimens in 0.5 M H_2SO_4 in the double layer region at different scanrates, ν . b) Determination of quasi-static capacity, here: $C = 33 \text{ mF}$ with a corresponding surface area of 840 cm^2 .

3.4.2 Sensing experiments

After the pre-deformation and determination of surface area, sensing experiments were performed. Therefore, the specimen was loaded to an elastic pre-strain $\varepsilon_0^* = 0.015$ by a static force $F_0 = -9.2 \text{ N}$ (negative-valued for compression), whereas the force amplitude \hat{F} was 2.85 N. The total applied strain was controlled at a constant frequency ω , with an additional elastic strain, ε^* , versus time, t , given by

$$\varepsilon^*(t) = \varepsilon_0^* + \hat{\varepsilon}^* \sin(\omega t) . \quad (3.12)$$

The strain amplitudes $\hat{\varepsilon}^*$ were varied from 0.001 to 0.0025. The resulting stresses (maximum applied stress of 11 MPa) were well below the yield stress, 21 MPa (see Fig. 3.13). For potential-response measurements ($\delta E/\delta \varepsilon$) as well as for current-response measurements ($\delta I/\delta \varepsilon$) a constant potential of 0.4 V was applied between sample (working electrode) and the pseudo reference electrode via a potentiostat.

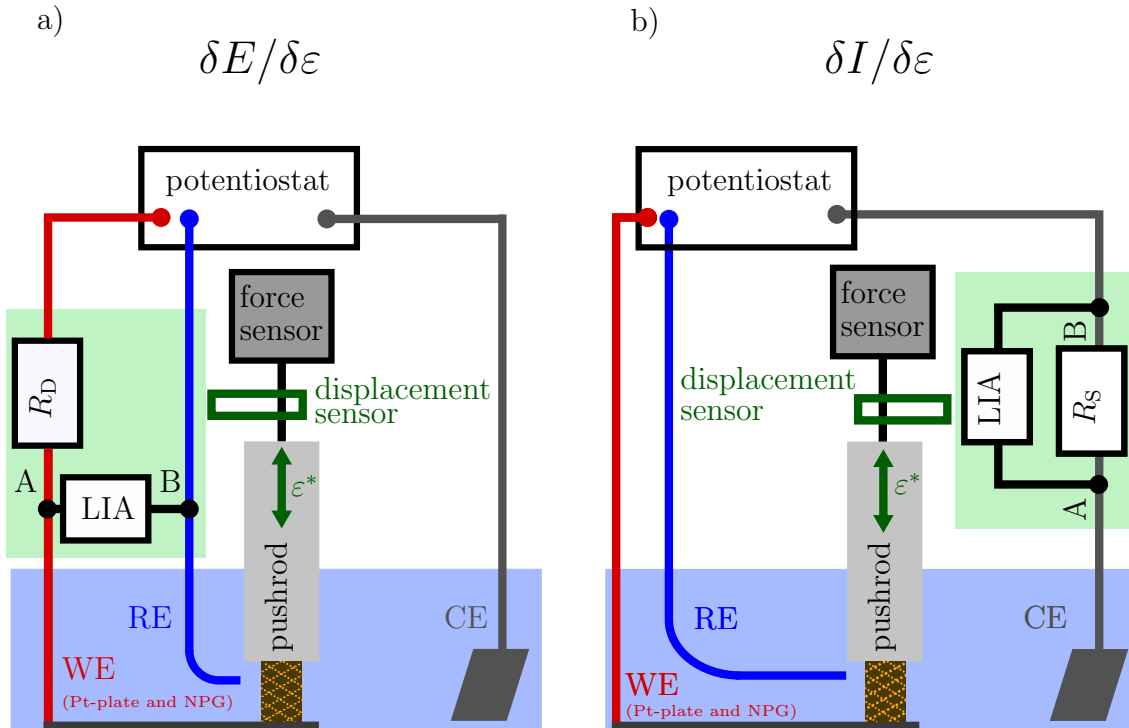


Figure 3.15: Schematic of *in situ* sensing measurement setup. Working electrode (WE) consisting of np-Au specimen on a platinum plate, reference electrode (RE), and counter electrode (CE) are immersed in electrolyte. All electrodes are connected to a potentiostat. The np-Au specimen is cyclically strained with an effective strain ε^* via the pushrod, force and displacement are measured simultaneously. a) Setup for potential-modulation measurement, $\delta E/\delta \varepsilon$: A Lock-In amplifier (LIA) is connected between WE and RE. R_D indicates the “delay resistance”, which is connected in series with potentiostat and WE. b) Setup for current-modulation measurement, $\delta I/\delta \varepsilon$: A LIA is connected parallel to the shunt resistance R_S , which is connected in series with potentiostat and CE. The connections of the LIA are denoted by “A” and “B”.

Electric signals were processed by a Lock-In amplifier (Oxford instruments/Stanford Research Systems) using the load cell signal of the DMA as the reference signal. A schematic of the measurement setup is shown in Fig. 3.15.

For potential-strain response measurements ($\delta E/\delta \varepsilon$) a “delay resistance” $R_D = 5 \text{ M}\Omega$ was inserted between working electrode and potentiostat, as indicated in a). Due to R_D the time constant of the control electronics is increased so that the compensation of the sensing potential variation is prevented [5]. The potential-strain response is sinusoidal, such as $E(t) = \hat{E} \sin(\omega t - \phi)$ where ϕ represents a phase shift with regard to the applied strain. The amplitude \hat{E} of the potential response to strain was determined via the Lock-

In amplifier (LIA) connected between working and reference electrode. The ports of the LIA are depicted as “A” and “B” in Fig. 3.15, here $E_{\text{input}} = E_A - E_B$. From the input potential E_{input} the LIA generates two direct-current (DC) signals (X and Y , see Section 3.2.6), proportional to the real ($E' \propto X$) and imaginary part ($E'' \propto Y$) of $E(t)$. Since the values are read out externally one has to convert the obtained signals as follows [56]:

$$E' = \frac{\sqrt{2} \times \text{sensitivity} \times X}{10 \text{ V}} . \quad (3.13)$$

A factor of $\sqrt{2}$ translates the signal from root mean square to the amplitude of the signal. The sensitivity of the LIA is connected to the amplitude of an input sine which results in a full scale DC output and can be set manually at the device. The 10 V correspond to the full scale of the output and has to be adjusted for each LIA type [56]. The amplitude of the potential variation can be calculated via

$$\hat{E} = \sqrt{E'^2 + E''^2} . \quad (3.14)$$

For current-strain response experiments, R_D was removed and a shunt resistance, $R_S = 47 \Omega$, connected in series with the counter electrode. The LI was connected parallel to R_S , as shown in Fig.3.15 b). The amplitude \hat{I} of the current-strain response was measured via the potential drop over the shunt resistance, R_S ,

$$\hat{I} = \left(\sqrt{I'^2 + I''^2} \right) / R_S . \quad (3.15)$$

3.4.3 Actuation experiments

For actuation experiments the *in situ* setup shown in Fig. 3.12 was exploited. The potential was swept cyclically from -0.1 V to 0.4 V vs the Ag/AgCl reference electrode with a scanrate of 2 mV s^{-1} (including the bias potential for sensing at 0.4 V). All experiments were performed in the capacitive part of the cyclic voltammogram (see Subsection 3.2.4), thus the chosen potential range was always below the potential for OH electrosorption, 0.75 V . The capacitive behavior in this potential range was confirmed via cyclic voltammetry. The electrocapillary coupling at gold surfaces is strongest near the potential of zero charge (*pzc*), [5, 63] which has been evaluated as $\approx 0.5 \text{ V}$ vs. SCE [64], this is $\approx 0.3 \text{ V}$ vs. our Ag/AgCl quasi RE, for Au (111) in solutions containing $\text{H}_2\text{SO}_4^{2-}$. Hence the *pzc* is within our potential scan range. During a potential sweep a constant compressive force of -0.5 N , resulting in a compressive stress of 0.11 MPa was applied. Simultaneously the effective strain ε^* is measured via DMA.

3.4.4 Machine stiffness

Since the DMA exhibits an inherent limited stiffness the raw measurement data had to be calibrated. Therefore, a measurement of stiffness with the empty electrochemical cell was performed, see Fig. 3.16. At a constant force F_0 oscillations with different amplitudes \hat{F}_{dyn} were applied and the resulting displacement amplitudes \hat{a}_{dyn} were recorded. From the slope of the resulting graph one can calculate the machine stiffness as 0.7 MN m^{-1} . All data in the following have been corrected with the corresponding machine stiffness.

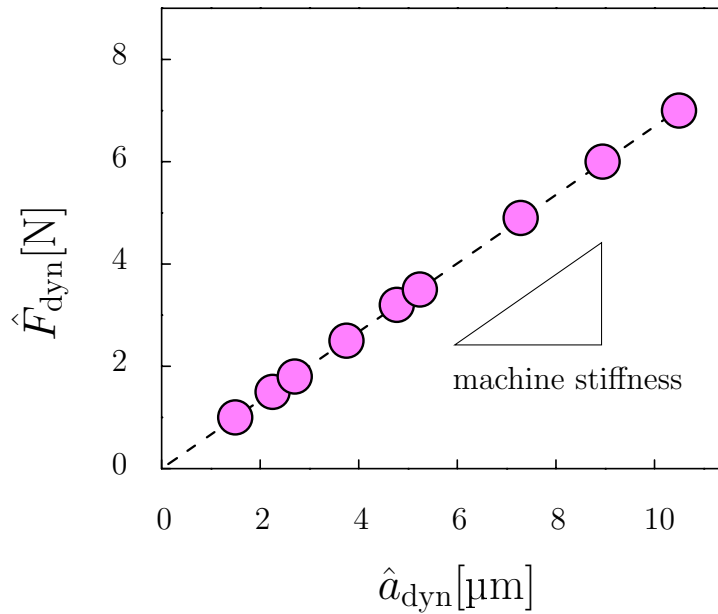


Figure 3.16: Dynamic force amplitude \hat{F}_{dyn} versus dynamic amplitude of displacement \hat{a}_{dyn} at a constant applied force of -9 N . The machine stiffness emerges as 0.7 MN m^{-1} from the slope of the curve in the linear range.

4 Results

4.1 Thermodynamical description of the system

4.1.1 Sensing-actuation relation

For the thermodynamical description of the system the microstructure is ignored and an effective medium is considered. V denotes the total sample volume (and pores) in the strain-free reference state and Q is the net electric charge. An uniaxial load F applied to the sample in direction of the longitudinal cylinder axis results in an uniaxial external traction, T (load per area of sample cross-section). Thus, mechanical work can be performed via the effective elastic linear strain ε^* in load direction. Suitable state variables for the net Helmholtz-type free energy \mathfrak{F} are ε^* and Q , as discussed in Section 2.2.1. \mathfrak{F} also depends on the constant V , therefore \mathfrak{F} can be expressed in terms of volume-specific quantities: $\mathfrak{F} = V\Psi(q^V, \varepsilon^*)$ with $q^V = Q/V$ the volume-specific charge and Ψ a free energy density function. The fundamental equation for Ψ is

$$d\Psi = Edq^V + Td\varepsilon^*. \quad (4.1)$$

To describe the actuation ability of the material an effective strain-charge coefficient A^* can be defined as

$$A^* = \left. \frac{d\varepsilon^*}{dq^V} \right|_T. \quad (4.2)$$

One can combine this equation with Eq. (2.10) to obtain the following relation:

$$A^* = -\frac{2\varsigma}{9K\varphi}\Theta \quad (4.3)$$

where ς is the electrocapillary coupling parameter, K is the bulk modulus and φ the volume fraction of the solid phase. Θ denotes a dimensionless parameter that depends on

Poisson's ratio, ν , and on the microstructure of the solid.

In the following instance of the triple product rule ¹

$$\left. \frac{dT}{dq^V} \right|_{\varepsilon^*} = - \left. \frac{dT}{d\varepsilon^*} \right|_{q^V} \left. \frac{d\varepsilon^*}{dq^V} \right|_T, \quad (4.4)$$

one can identify the effective potential-strain coupling coefficient (potential variation per strain at open circuit),

$$\zeta^* = \left. \frac{dE}{d\varepsilon^*} \right|_{q^V}, \quad (4.5)$$

via the following Maxwell relation

$$\left. \frac{dT}{dq^V} \right|_{\varepsilon^*} = \left. \frac{dE}{d\varepsilon^*} \right|_{q^V}. \quad (4.6)$$

The effective Young's modulus Y^* is defined at open circuit as

$$Y^* = \left. \frac{dT}{d\varepsilon^*} \right|_{q^V}. \quad (4.7)$$

Thus, one can write Eq (4.4) as

$$\zeta^* = -Y^* A^*. \quad (4.8)$$

Equation (4.8) was derived from the fundamental equation (4.1) without further assumptions. It relates the potential-strain coupling coefficient ζ^* to the actuation coefficient A^* via the effective Young's modulus. Via this equation one can estimate the magnitude of electric sensing signals (ζ^*) generated in response to load from actuation experiments (A^*). In addition, Y^* offers further insight into the issue of local versus macroscopic/effective strain in porous media.

4.1.2 Charge-load coupling parameter and the corresponding piezoelectric coefficient

The coupling between net charge on a nanoporous body and strain can be estimated from the following approach: Whereas $C = dQ/dE$ denotes the *net* differential sample capacity, $c = dq^A/dE$ identifies the *local* differential capacitance (capacity per area) of the metal surface. Thus, the coupling of net charge and strain emerges as

$$\left. \frac{dQ}{d\varepsilon^*} \right|_E = - \left. \frac{dQ}{dE} \right|_{\varepsilon^*} \left. \frac{dE}{d\varepsilon^*} \right|_Q = -C\zeta^* = c\alpha\varphi V Y^* A^* \quad , \quad (4.9)$$

¹as stated in Ref. [65]: $\left. \frac{dX}{dY} \right|_Z = - \left. \frac{dX}{dZ} \right|_Y \left. \frac{dZ}{dY} \right|_X$

with φ the solid fraction and α , the the specific surface area (area S per volume of the solid phase, V_{solid} , i.e. $S/\varphi V$). As indicated above, the charge transferred per strain scales with the actuator volume, V .

From the following equations the respective coupling strength, i.e. the *charge-load coefficient* for a cylindrically shaped nanoporous body (cross-sectional area A_S and height l_0) is derived:

$$\left. \frac{dQ}{dF} \right|_E = \frac{1}{A_S} \left. \frac{dQ}{dT} \right|_E = \frac{1}{A_S} \left. \frac{dQ}{d\varepsilon^*} \right|_E \left. \frac{d\varepsilon^*}{dT} \right|_E \quad (4.10)$$

Combining equation (4.10) with equation (4.9) and the approximation $^2 Y^* = \left. \frac{dT}{d\varepsilon^*} \right|_{q^V} \approx \left. \frac{dT}{d\varepsilon^*} \right|_E$ the following expression for the charge-load coupling coefficient is obtained:

$$\left. \frac{dQ}{dF} \right|_E \approx -\frac{c\alpha\varphi\zeta^*}{Y^*} l_0 \quad , \quad (4.11)$$

where the volume of the specimen is substituted by $V = A_S l_0$ and equation (4.8) is applied.

Equations 4.9 and 4.11 suggest that the charge per strain in a nanoporous metal scales with volume and the charge per load scales with the thickness of the material, respectively.

In order to further compare piezoelectric to nanoporous-metal sensors the longitudinal piezoelectric coefficient d_{33} is introduced. Under conditions of a small electric field, the constitutive relations for a piezoelectric material are [66]

$$\begin{bmatrix} \mathbf{D} \\ \varepsilon \end{bmatrix} = \begin{bmatrix} \mathbf{e}^T & \mathbf{d}^d \\ \mathbf{d}^c & \mathbf{s}^E \end{bmatrix} \begin{bmatrix} \mathbf{E} \\ T \end{bmatrix} \quad , \quad (4.12)$$

where \mathbf{D} , with a size of (3×1) , denotes the electric displacement, ε is strain (6×1) , \mathbf{E} is the applied electric field (3×1) , and T indicates the stress (6×1) . The dielectric permittivity \mathbf{e}^T (3×3) , the piezoelectric coefficients \mathbf{d}^d (3×6) and \mathbf{d}^c (6×3) , and the elastic compliance \mathbf{s}^E of size (6×6) are the piezoelectric constants. The piezoelectric coefficient \mathbf{d}^c gives strain per unit field at constant stress and \mathbf{d}^d gives electric displacement per unit stress at constant electric field. The superscripts \mathbf{c} and \mathbf{d} indicate the difference between the converse (actuation) and direct (sensing) piezoelectric effects, in practice, however, these coefficients are numerically equal. The superscripts T and \mathbf{E} imply that the corresponding parameter is measured at constant stress or constant electric field, respectively. Equation 4.12 can be simplified to describe the sensing effect in piezoceramics.

²It can be shown that the closed- and open-circuit Young's moduli are related by $\left. \frac{dT}{d\varepsilon^*} \right|_E = \left. \frac{dT}{d\varepsilon^*} \right|_{q^V} - c^V(\zeta^*)^2$. With the experimental data for the volume-specific capacitance c^V and for the coupling coefficient ζ^* of our material, the two elastic constants are found differ relatively by less than 10^{-4} .

The material is exposed to a stress field and generates a charge in response. When the applied external electric field E is zero, Eq. 4.12 can be expressed as follows [66]:

$$\begin{bmatrix} D_1 \\ D_2 \\ D_3 \end{bmatrix} = \begin{bmatrix} 0 & 0 & 0 & 0 & d_{15} & 0 \\ 0 & 0 & 0 & d_{24} & 0 & 0 \\ d_{31} & d_{32} & d_{33} & 0 & 0 & 0 \end{bmatrix} \begin{bmatrix} T_1 \\ T_2 \\ T_3 \\ T_4 \\ T_5 \\ T_6 \end{bmatrix} \quad (4.13)$$

where the coefficients d_{31} , d_{32} and d_{33} connect the normal strain in 1, 2, and 3 (i.e. x , y , and z) direction parallel to the poling axis, respectively. The coefficients d_{15} and d_{24} are related to shear strain. This equation depicts the principle of the piezoelectric sensing effect. A stress field T induces an electric displacement \mathbf{D} as a result of the direct piezoelectric effect [66].

The figure of merit for comparison with a nanoporous-metal sensor is the coefficient d_{33} in longitudinal direction. d_{33} is defined as charge displaced per load, F , (unit: $[\text{C N}^{-1}]$, with $F = A_S T$ where A_S denotes the cross-sectional area), thus it is the equivalent parameter of $dQ/dF|_E$ of a nanoporous-metal hybrid materials. In that case (i.e. an isotropic piezoceramic under uniaxial load in z -direction) Eq. 4.13 simplifies to $D_3 = d_{33}T_3$.

As indicated in eq. (4.11) the charge-load coefficient of a nanoporous body scales with its thickness. Thus, the charge-load coefficient can be tailored via geometry, whereas d_{33} of a piezoceramic is independent of the geometry.

4.2 Experimental results

4.2.1 Actuation with nanoporous gold

Actuation experiments were performed on millimeter-sized, cylindrically-shaped nanoporous gold specimen infiltrated with electrolyte in a DMA test machine setup as shown in Fig. 3.12. The samples were exposed to a constant compressive stress by the pushrod to obtain contact while the potential was swept cyclically. Simultaneously the resulting effective strain ε^* was measured *in situ*. For more detailed information, see Subsection 3.4.3.

Representative results of one measurement cycle on one sample for electrochemical actuation are shown exemplarily in Fig. 4.1. During each measurement cycle, five subsequent potential scans (-0.1 V to 0.4 V at scan rate 2 mV s^{-1}) were performed while the effective strain ε^* and resulting charge Q were recorded simultaneously. As shown in fig. 4.1, the sign of the potential–strain coupling, expansion during positive-going potential scans and contraction during negative-going potential scans agrees with previous experiments on nanoporous gold [34, 67, 68].

From actuation measurements the effective strain-charge coefficient A^* was calculated via Eq (4.2). Therefore, the data from Fig. 4.1 was averaged over the performed 5 potential sweeps, separately for positive and negative-going sweeps and the resulting effective strain, ε^* , and volumetric charge density, q^V were determined. The obtained data is shown in Fig. 4.2, in which the averaged strain versus q^V is plotted. Via linear regression of this data the actuation parameter $A^* = (0.0471 \pm 0.0004)\text{ mm}^3\text{ C}^{-1}$ is calculated. On average over the three samples in this study $A^* = (0.0475 \pm 0.0010)\text{ mm}^3\text{ C}^{-1}$ is found. An excellent sample-to-sample reproducibility is implied by the small variance.

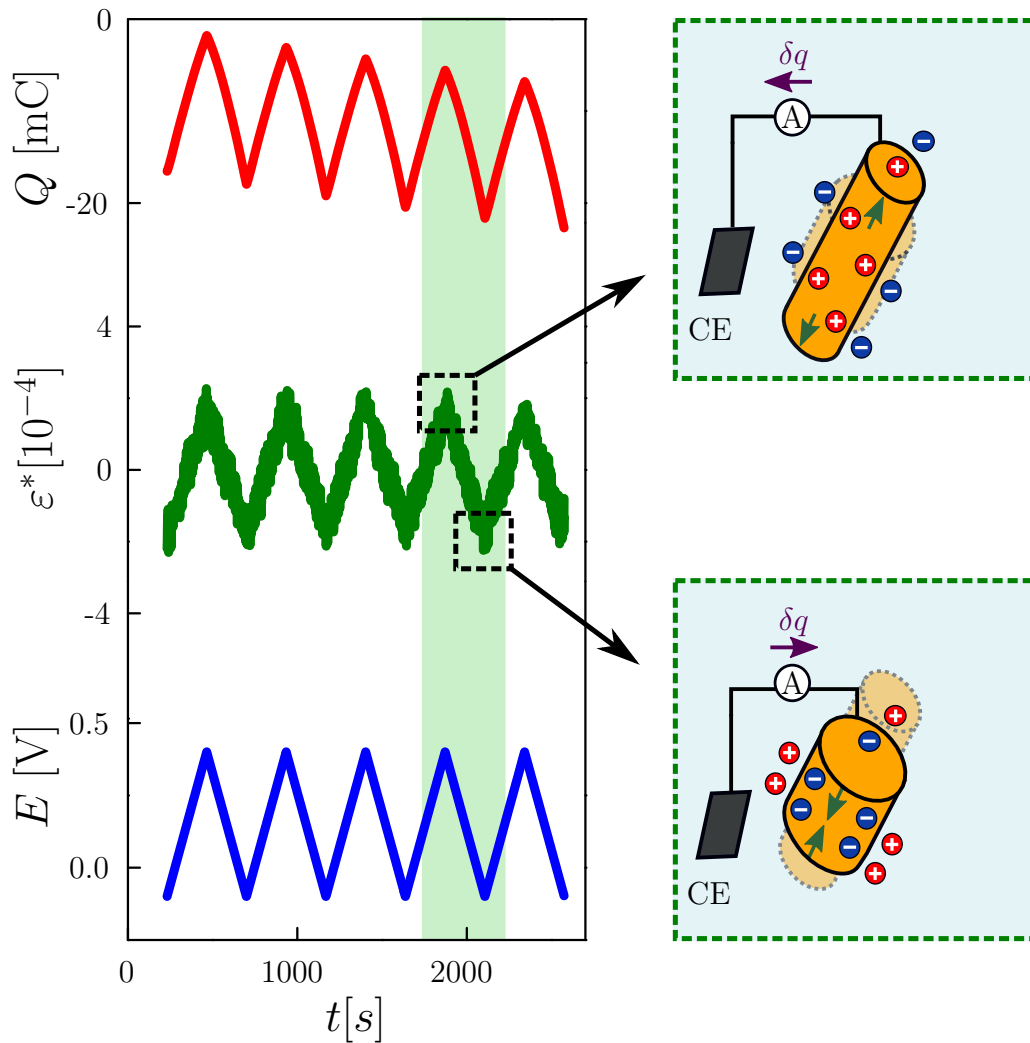


Figure 4.1: Actuation measurement. *Left:* Five representative potential sweeps on one specimen. Increasing or decreasing the potential (lower part, blue line, measured vs. a Ag/AgCl pseudo-reference electrode) leads to an increase or decrease of the effective strain ε^* (middle, green line) and the charge Q (upper part, light red line), respectively. Sketches on the *right* illustrate the electromechanical coupling corresponding to elongation (*above*) and contraction (*below*) of a wire-shaped ligament. Adapted from Stenner *et al.*, see Ref. [42].

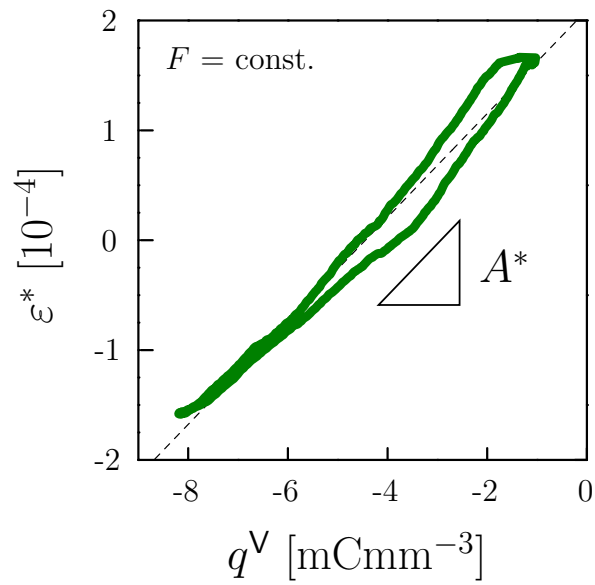


Figure 4.2: Averaged effective-strain ε^* versus volumetric charge density q^V for the data of 4.1. Dashed black line represents linear fit. Adapted from Stenner *et al.*, see Ref. [42].

4.2.2 Strain-sensing with nanoporous gold: Proof of principle

For sensing experiments the sample was exposed to a cyclic strain with an effective amplitude $\hat{\varepsilon}^*$ at a constant offset of ε_0^* . The corresponding electrical signals were recorded at a constant electrode potential of $E = 0.4$ V vs. the Ag/AgCl pseudo-reference electrode, i.e. in the capacitive regime. More experimental details can be found in Subsection 3.4.2. Figure 4.3 shows oscilloscope traces for two separate sensing experiments at a constant

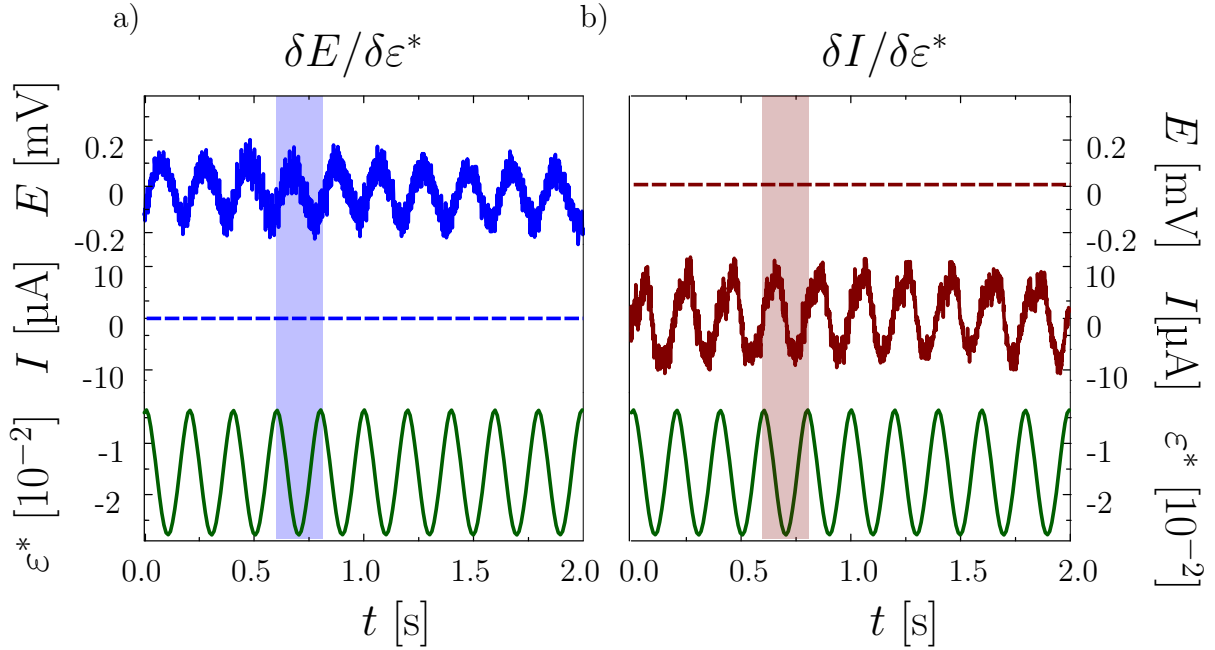


Figure 4.3: Measurement signals obtained via an oscilloscope. The potential E is modulated (straight blue line) by an applied effective strain ε^* (green line) with a frequency of 5 Hz, while the current I is constant (dashed blue line). b) The current I is modulated (straight red line) by an applied effective strain ε^* (green line) with a frequency of 5 Hz, while the current E is constant (dashed red line). Data has been published by Stenner *et al.*, see Ref. [42].

frequency. The measurements are representative and were obtained without further amplification, nevertheless, the oscilloscope exhibits a high input impedance (1 M Ω). To determine the potential variation with strain, $\delta E / \delta \varepsilon^*$ (see Fig 4.3 a)), the strain was modulated at a frequency of $\omega / 2\pi = 5$ Hz, and the potential variation was recorded under conditions of zero current. Strain amplitudes in the order of 1% induce variations in potential with amplitudes in the order of 100 μ V. The potential variation seems to be phase shifted by 180° with respect to the strain. However, in Ref. [69] the observed phase shift from straining planar gold electrodes is discussed as follows:

As stated before, $\varsigma^* = \hat{E} / \hat{\varepsilon}^*|_{qV}$ and the applied strain follows $\varepsilon^*(t) = \varepsilon_0^* + \hat{\varepsilon}^* \sin(\omega t)$. The static strain ε_0^* is negligible in the following. We can summarize both equations to

$$E(t) = \varsigma^* \varepsilon^* \sin(\omega t + \Theta_E) \quad (4.14)$$

which is equivalent to

$$E(t) = \zeta^{*'} \varepsilon^* \sin(\omega t) + \zeta^{*''} \varepsilon^* \cos(\omega t) \quad (4.15)$$

where the real and imaginary part of the experimental potential-strain coupling coefficient are denoted as $\zeta^{*'}$ and $\zeta^{*''}$, respectively. Thus, Θ_E is calculated as

$$\tan(\Theta_E) = \frac{\zeta^{*''}}{\zeta^{*'}} \quad (4.16)$$

In this convention, which is equivalent to the data evaluation in this work, a delayed response is indicated by oppositely-signed values of $\zeta^{*'}$ and $\zeta^{*''}$ as well as a negative phase shift Θ_E . Since ζ^* of nanoporous gold is negative, the signal appears phase-shifted by 180° .

To determine the current variation with strain, $\delta I / \delta \varepsilon^*$ (see Fig 4.3 b)), the strain was modulated at the same frequency as above (5 Hz), and the current variation was recorded under conditions of zero potential. Strain amplitudes in the order of 1% induce current variations, with amplitudes in the order of 10 μ A.

4.2.3 Strain-sensing with different strain amplitudes

Sensing experiments with different applied strain amplitudes at the same frequency were performed to characterize the coupling between potential (current) and strain. At a constant prestrain of $\varepsilon_0^* = 0.015$ the specimen was deformed cyclically with strain amplitudes $\hat{\varepsilon}^*$ varying from 0.001 to 0.0025 at a frequency of $\omega/2\pi = 20$ Hz. The amplitude \hat{E} of the potential response was recorded simultaneously to the strain oscillation, afterwards the amplitude of the current response \hat{I} was recorded *in situ* in the setup shown in Fig. 3.15. Both signals were obtained via a lock in amplifier and processed as discussed in Subsec. 3.4.2.

The results of repeated measurements on six samples are compiled in Fig. 4.4. A linear variation in both, potential and current amplitudes, as well as a high sample-to-sample reproducibility is found in these measurements. The set of data shown in the graph consists of calibrated data of three specimens already published in 2016 by Stenner *et al.* [42] and repeated measurements on three identically synthesized specimens in 2018. Note the very good sample-to-sample reproducibility.³

The data displayed in Fig. 4.4 suggest an effective potential-strain coupling parameter $\zeta^* = \hat{E} / \hat{\varepsilon}^*|_{q,v}$ of (-46.4 ± 1.3) mV. To validate whether the signal strength from the above

³The deviation from the data published in 2016 (see Ref. [42]) is due to a measurement procedure improvement. The here-presented values have been calibrated with the machine stiffness (whereas those in Ref. [42] have not been calibrated) and exhibit a higher ε^* than the published data. The data points from 2016, which have been retrospectively corrected agree very well with the new data from 2018.

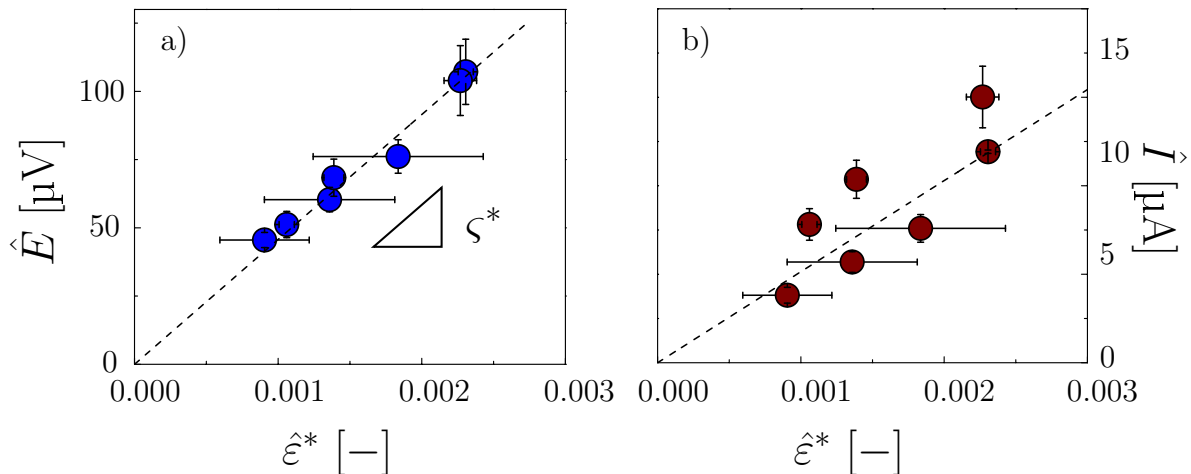


Figure 4.4: Electric signals from sensing experiments with strain amplitude variation at frequency $\omega/2\pi = 20$ Hz. (a) Potential amplitude \hat{E} versus strain amplitude $\hat{\epsilon}^*$. Effective strain-potential coupling parameter ζ^* can be calculated from slope of the curve, as indicated by the triangle. (b) Current amplitude \hat{I} versus strain amplitude $\hat{\epsilon}^*$. Black dashed lines indicate linear fits.

described sensing experiments at 20 Hz is quantitatively consistent with the quasi-static actuation measurement Eq (4.8) is explored. It links sensing experiments to actuation via the effective Young's modulus. Before each sensing cycle and each actuation experiment the effective Young's modulus Y^* was determined as the storage modulus in the DMA. Y^* remained constant during the measurements and the average over all samples was $Y^* = (900 \pm 100)$ MPa.

As basis for the validation the potential-strain coupling parameter ζ^* is taken into account. Equation (4.8) indicates that the parameter can be either calculated from sensing experiments (as the strain-derivative of the potential at constant charge (Fig. 4.4 (a)), or from actuation experiments (as the product of effective Young's modulus and actuation coefficient (Fig. 4.2)).

The small variances in ζ^* underline the high sample-to-sample reproducibility, even between two different batches of samples. The coefficient determined from sensing, $\zeta^* = \hat{E}/\hat{\epsilon}^*|_{qV} = (-46.4 \pm 1.3)$ mV, yields excellent agreement with the one determined from actuation, $\zeta^* = -Y^*A^* = (-42.8 \pm 5.7)$ mV. Both values coincide within their errors. This observation provides strong support for the analysis of sensing and actuation mechanism in terms of electrocapillary coupling, see Section 2.2, and will be discussed in the following Chapter.

The net quasi-static capacity, $C = (51.2 \pm 3.0)$ mF, and the net surface area, $S \approx 1280$ cm, calculated from C , (see Chapter 3) were determined to characterize the specimens and check the sample-to-sample comparability. All samples had identical mean ligament size, the different variance in C is consistent with slightly different macroscopic volumes and lies

within the error of sample volume determination. The capacity per volume is $\approx 20 \text{ F cm}^{-3}$ consistent with previous reports on np-Au based supercapacitors [70]. The high net capacities of 40–50 mF emphasize the extremely large internal surface area and the abundance of polarizable sites in the hybrid material.

The data shown above was obtained via alternating sensing and actuation measurements, and only interrupted by determination of the Young's modulus via DMA. The measurement cycles were repeated 5 times for each sample, the samples were not removed from the electrochemical cell during the experiment. The investigation of each specimen consists of 1.2×10^5 load cycles in sensing plus 25 actuation cycles. Quasi-static measurements indicate that the surface areas were reduced by $\approx 30\%$ after the investigation.

4.2.4 Dependence of potential- and current responses on strain-frequency

It is also of interest in how far the induced potential change and the resulting charge transfer is affected by the frequency of the excitation. Therefore the applied frequency $f = \omega/2\pi$ was swept from 0.5 Hz to 100 Hz at constant strain amplitude. Three specimens were repeatedly measured for determination of the following data.

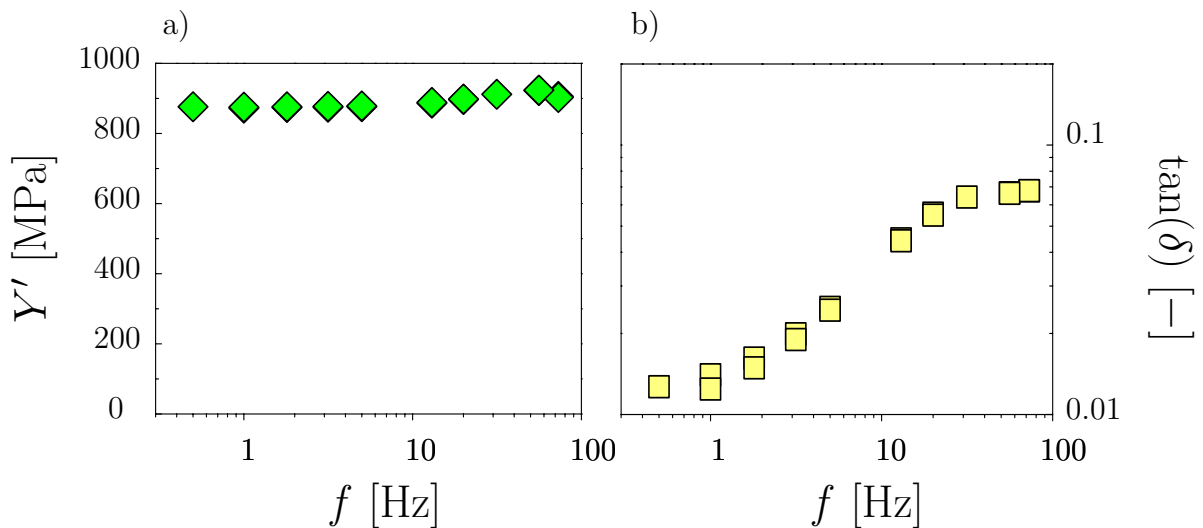


Figure 4.5: Dynamic mechanic analysis measurements performed at constant effective strain amplitude $\hat{\varepsilon}^*$. a) Storage modulus Y' versus applied frequency, $f = 2\pi/\omega$. b) Phase shift $\tan(\delta)$ between applied load and strain versus f .

Figure 4.5 depicts representative DMA results obtained from one sample by sweeping the frequency up to 100 Hz and back to to 0.5 Hz. The storage modulus Y' is constant from 0.5 to 100 Hz, as shown in a). The phase shift δ between applied load and induced strain in that frequency range is very small ($\delta \leq 4.3^\circ$) and constant for frequencies below 10 Hz,

see b). The results point towards a reliable and stable measurement in the range of 0.5 to 100 Hz.

The frequency sweeps at constant prestrain of $\varepsilon_0^* = 0.015$ and a strain amplitude of $\hat{\varepsilon}^* = 0.0025$ were performed simultaneously with the DMA tests shown above. All sensing results were obtained via a Lock-In amplifier as described in Subsection 3.4.2.

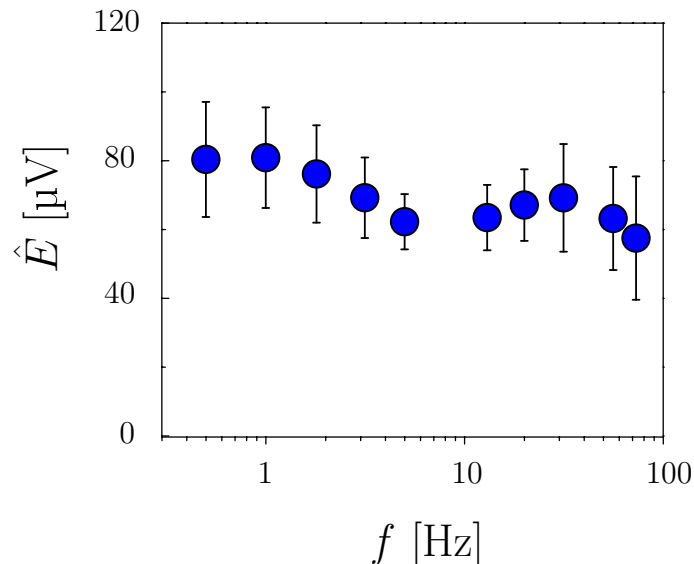


Figure 4.6: Potential response from sensing experiments with frequency variation at constant strain amplitude. Symbols indicate potential amplitude \hat{E} versus frequency $f = \omega/2\pi$.

As indicated in Fig. 4.6 the amplitude of potential modulation \hat{E} tends to stay constant within the variance over the frequency range of the experiment. The same observation is made for the amplitude of the current modulation \hat{I} , see Fig. 4.7 a) (dark red symbols). The bright red symbols indicate a measurement performed with the impedance spectroscopy module of the potentiostat, where a potential modulation with an amplitude $\hat{E} = 100 \mu\text{V}$ was applied to the specimen. The frequency of this modulation was swept from 1 to 90 Hz and the resulting oscillation of current was recorded (see Subsec. 3.2.5). This corresponds to a purely electrochemical excitation without mechanical influences. In the investigated frequency range both data agree well, however, the impedance data suggests an increase in amplitude with increasing frequency for $f \geq 50$ Hz. The slightly higher absolute values of the impedance data originate from the higher potential modulation amplitude: As shown in Fig. 4.6 the amplitude of the induced potential response, \hat{E} , obtained from sensing experiments is $\approx 80 \mu\text{V}$, whereas \hat{E} in the impedance experiment was set to $100 \mu\text{V}$.

In Fig. 4.7 b) the phase shift, Θ_I , between the potential oscillation imposed by the impedance module and the resulting current of one representative measurement is shown.

The mean phase shift between strain and current over the frequency range of the experiment can be estimated as $(-10 \pm 5)^\circ$, assuming an negligible phase shift Θ_E between strain and potential as indicated by the oscilloscope traces and the discussion in Subsec. 4.2.2.

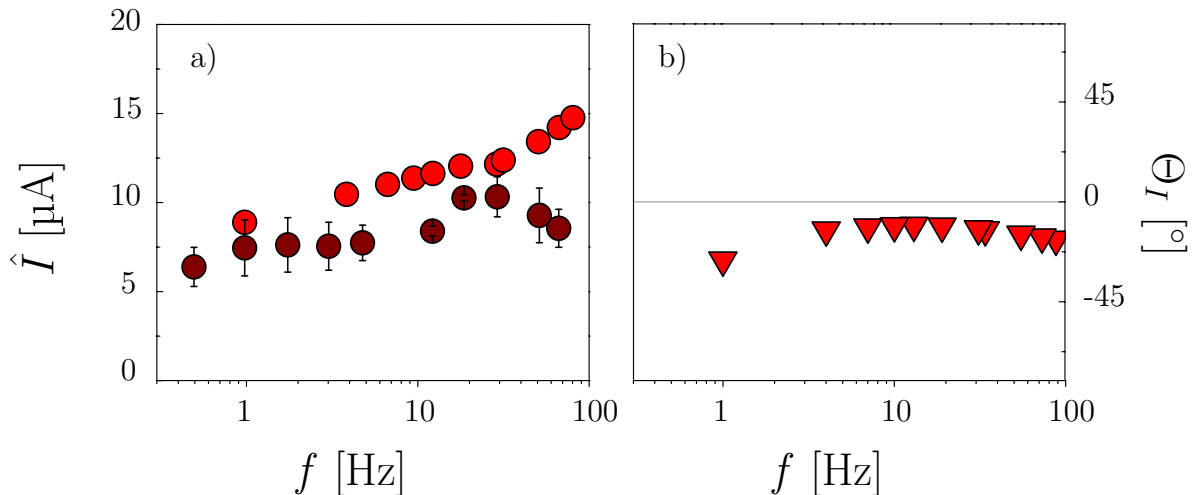


Figure 4.7: Current responses from sensing and impedance-spectroscopy experiments with frequency variation at constant strain/potential amplitude. a) Current amplitude \hat{I} versus frequency $f = \omega/2\pi$. Dark red symbols indicate response-signals from sensing experiments and bright red symbols indicate impedance spectroscopy data. The impedance data was obtained by applying a potential variation $\hat{E} = 100 \mu\text{V}$ comparable to $\hat{E} \approx 80 \mu\text{V}$ measured in sensing experiments. b) Phase shift between potential and current Θ_I determined via impedance spectroscopy.

Fig. 4.8 displays the charge amplitude \hat{Q} over the applied frequency f . The sensing data (purple symbols) agree well with data from impedance spectroscopy (pink symbols). A decrease of charge transfer with increasing frequency is observed. An explanation for this observation can be found in the ionic transport resistance in the pores of the specimen. For further confirmation of this behavior quasi-static measurements (cyclic voltammetry) as well as sensing and impedance-spectroscopy experiments at 20 Hz were performed. As a suitable parameter for comparison the effective capacity C was determined.

The potentiostat's impedance module was used to impose a potential modulation to measure an effective capacity from the ratio of current- and potential amplitudes (see Subsection 3.2.5, $C = \hat{I}/\omega\hat{E}$). For an applied frequency of 20 Hz a capacity of $C_{20\text{Hz}; \text{EIS}} = 1.02 \text{ mF}$, 50 fold less than the quasi-static capacity ($C_{\text{quasi static}} \approx 50 \text{ mF}$) was found. The quasi-static capacity was measured via cyclic voltammetry, see Section 3.4.

To determine the effective capacity from strain-sensing experiments at 20 Hz, a strain modulation was applied and \hat{I} (at constant E) as well as \hat{E} (at constant Q) were measured separately. From the ratio of both values $C_{20\text{Hz}; \text{sensing}}$ was calculated as 0.88 mF.

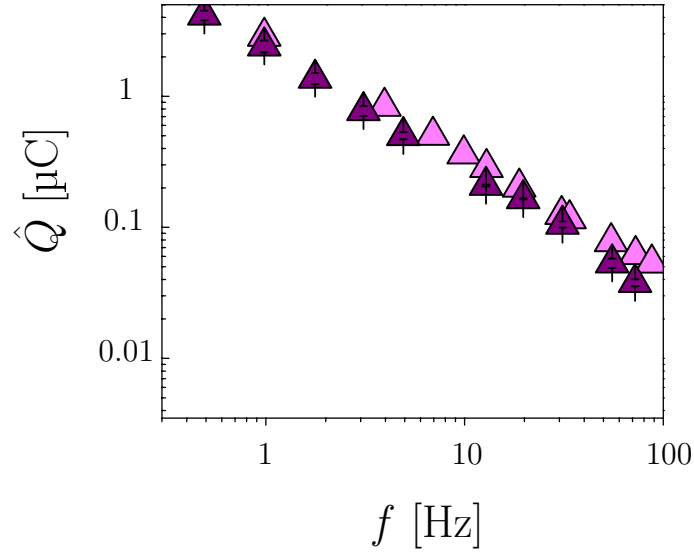


Figure 4.8: Charge response amplitude \hat{Q} from sensing and impedance-spectroscopy experiments with frequency variation at constant strain/potential amplitude. Purple symbols indicate response-signals from sensing experiments and pink symbols indicate impedance spectroscopy data. The impedance data was obtained by applying a potential variation $\hat{E} = 100 \mu\text{V}$ comparable to $\hat{E} \approx 80 \mu\text{V}$ measured in sensing experiments.

Both capacity values at 20 Hz, $C_{20\text{ Hz}; \text{sensing}}$ and $C_{20\text{ Hz}; \text{EIS}}$, agree well. This consistency shows that the reduced charge transfer of the sensor at high frequencies is a result of the electrochemical impedance, which can be understood as an ionic transport resistance in the pores.

4.2.5 Charge-load coupling at finite and quasi-static frequencies

The coupling, $dQ/dF|_E$, between net charge on the sample and external load near equilibrium was explored in a quasi-static sensing experiment at a very low frequency. The sample was prestrained by a static force $F_0 = -9.2 \text{ N}$ (negative-valued for compression, corresponds to a static compression stress of 8.1 MPa) and the load was modulated at frequency 10 mHz with a force amplitude of 2.9 N (stress amplitude of 2.5 MPa).

Figure 4.9 shows that the charge varies linearly with strain. Linear regression yields $dQ/dF|_E = (1.933 \pm 0.003) \mu\text{C N}^{-1}$. From the corresponding measurements at 20 Hz $dQ/dF|_E$ was calculated from the load- and current amplitudes of Fig. 4.4 (b) as 34 nC N^{-1} . From Eq (4.11) $dQ/dF|_E$ using ζ^* and $C_{20\text{ Hz}}$ from the sensing experiment yields $dQ/dF|_E = 84 \text{ nC N}^{-1}$, again in the same order of magnitude.

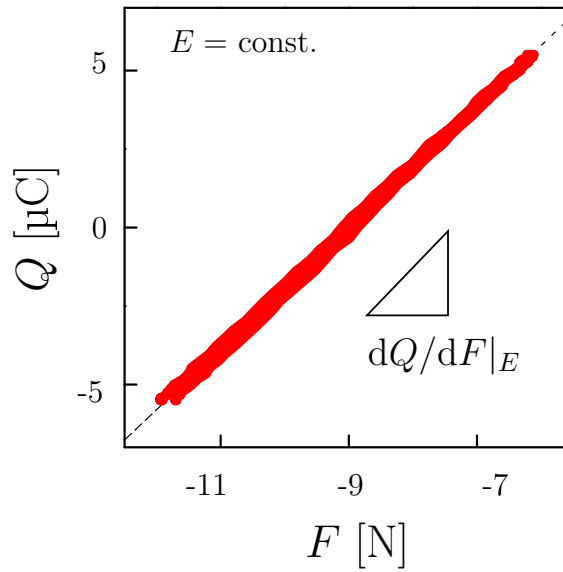


Figure 4.9: Quasi static sensing experiment performed at a frequency of 10 mHz at constant applied potential. The charge increases linearly with applied force (red line). Linear fit is indicated via dashed black line. Adapted from Stenner *et al.*, see Ref. [42].

4.2.6 Dependence of potential- and current responses on connectivity density and ligament size

To investigate the influence of structural properties of the nanoporous specimen on the effective electromechanical coupling parameters experiments on samples with different ligament sizes L and different connectivity of ligaments were performed. The *connectivity* is a topological characteristic and describes the number of non-redundant handles within a three-dimensional body. Since the connectivity itself depends on the volume of the sample, a more meaningful parameter, the connectivity density (i.e. connectivity divided by volume), is introduced and multiplied by a cubed structural size measure to normalize the parameter with the length scale of the structure. For samples prepared from $\text{Au}_{25}\text{Ag}_{75}$ precursors the scaled connectivity density is found to be proportional to the inverse cubed ligament size, L^{-3} , in finite element simulations and thus decreases with increasing ligament size L [71]. The dependence of the connectivity density on the precursor alloy composition was investigated via finite element simulation by Soyarslan *et al.*, see Ref. [48]. The results point towards an increase in connectivity density with increasing gold amount in the master alloy.

The samples were prepared from different master alloys, $\text{Au}_{30}\text{Au}_{70}$ and $\text{Au}_{25}\text{Au}_{75}$, of which one batch was thermally annealed (see Sec. 3.3). The three different types of samples are compiled in the SEM micrographs in Fig. 4.10, the expected/measured increase/decrease in connectivity density/ligament size is indicated by the arrows, respectively.

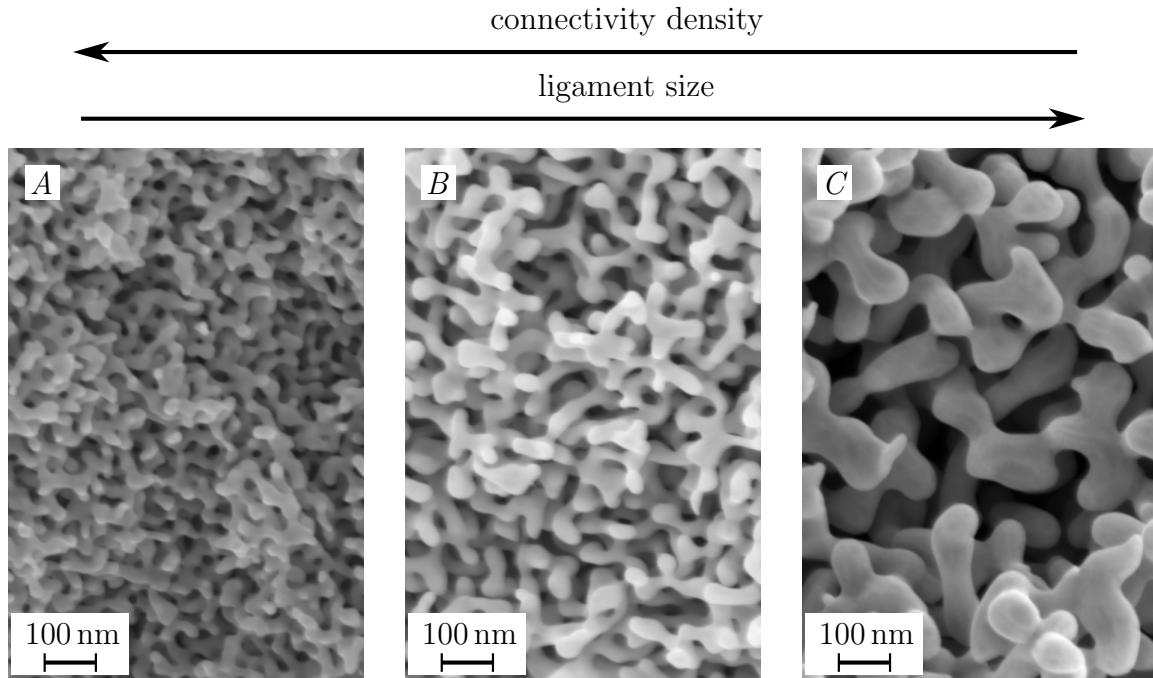


Figure 4.10: Scanning electron micrographs of nanoporous gold samples with different ligament sizes and network connectivity densities. As indicated by arrows the connectivity density increases from *left to right*, whereas the ligament size decreases, respectively. All surfaces shown are fracture surfaces. *A*: Specimen with high expected connectivity density prepared from $\text{Au}_{30}\text{Au}_{70}$ master alloy with a ligament size of approximately 30 nm. *B* and *C*: Specimen with lower connectivity density prepared from $\text{Au}_{25}\text{Au}_{75}$ master alloy. Ligament sizes of approximately 40 nm and 100 nm, respectively.

The increase in connectivity density is indicated by the effective Young’s modulus, Y^* which is 1700 MPa, 900 MPa, and 400 MPa of samples *A*, *B*, and *C*, respectively. Due to the resulting increase in strength and the difficulty of a perfect parallel alignment of the measurement setup and the samples, specimens *A* were predeformed only to a maximum strain of 0.08. Above this value failure of the samples was observed in the electrochemical setup. The increase in Y^* might also be influenced by the decrease in ligament size L (“smaller is stronger”) [44].

The electrochemical measurements, however, exposed surprising results that will be presented here and discussed in the following Chapter. The quasi-static capacity C of samples *A* and *B* yielded ≈ 50 mF for both samples, which indicates a comparable electrochemical surface area of ≈ 1200 cm². Via energy-dispersive X-ray spectroscopy the amounts of

residual silver were determined as ≤ 1 at.% in specimens *B* and *C*, whereas *A* presented a very high amount of 5 at.%. The results of sensing experiments performed on the three different types of specimens are compiled in Fig. 4.11. The samples were pre-strained with a static strain of $\varepsilon^* = 0.015$ and cyclically strained at a frequency of 20 Hz. The effective strain amplitudes $\hat{\varepsilon}^*$ were varied between 0.001 and 0.0043. Each data point is the result of averaging measurements that were performed repeatedly on three samples. The values of specimens *B* have already been presented and discussed in Subsec. 4.2.3.

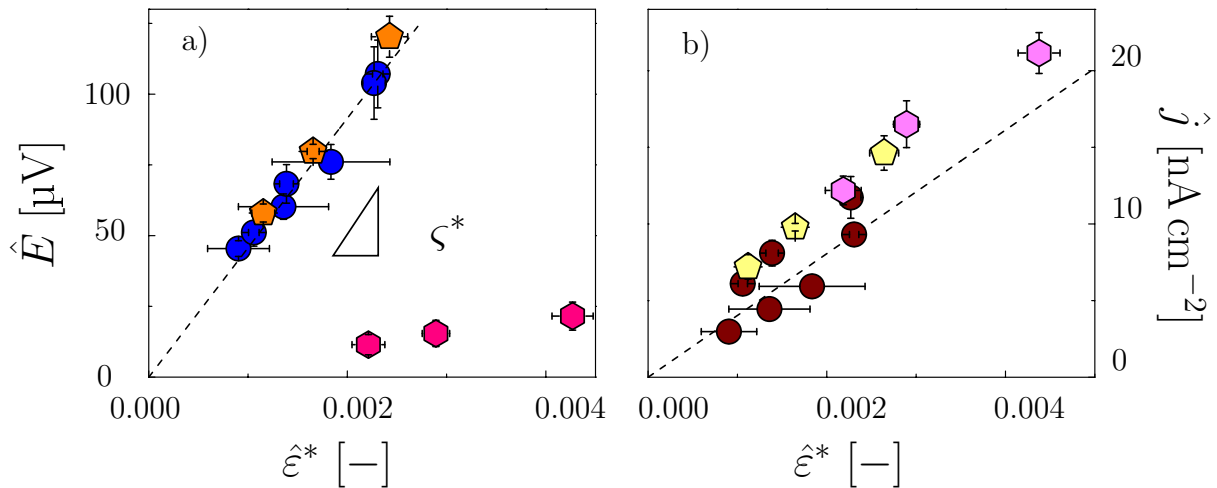


Figure 4.11: Electric signals from sensing experiments with strain amplitude variation at frequency $\omega/2\pi = 20$ Hz. a) Potential amplitudes \hat{E} versus strain amplitude $\hat{\varepsilon}^*$. Effective strain-potential coupling parameter ζ^* can be calculated from slope of the curve, as indicated by the triangle. Orange pentagons, blue circles, and pink hexagons indicate data of specimen *A*, *B*, and *C*, respectively. Black dashed line indicates linear fit of results from specimens *B*. b) Current density amplitudes \hat{j} versus strain amplitude $\hat{\varepsilon}^*$. Yellow pentagons, blue dark red, and violet hexagons indicate data of specimens *A*, *B*, and *C*, respectively. Black dashed line indicates linear fit of results from specimens *B*.

Figure 4.11 a) shows the potential responses to strain of the three different types of samples. *C* exhibits a low potential response ($\zeta_C^* = dE/d\varepsilon^*|_q \approx -5$ mV) as expected, due to its small surface area and low connectivity density [45, 71]. Since specimens *A* and *B* exhibit comparable ligament sizes but different network connectivity densities, a higher potential-strain coupling parameter ζ^* is expected for sample *A* as a result of higher connectivity density. However, the values $\zeta_A^* = (-49.0 \pm 0.6)$ mV and $\zeta_B^* = (-46.4 \pm 1.3)$ mV nearly coincide.

Figure 4.11 b) shows the current responses normalized to the sample surface for the different specimens. The normalized current-strain response parameters $d\hat{j}/d\varepsilon^*|_E$ approximately coincide, since the data points are nearly positioned on a line. This leads to the conclusion that the current response is proportional to the surface area S and that by increasing S one might directly be able to increase \hat{I} .

5 Discussion

5.1 Quantification of sensing-actuation relation

Nanoporous gold (np-Au) specimens imbibed with electrolyte respond to elastic mechanical deformation by exhibiting readily measurable potential changes and by actively generating electric current, similarly to piezoelectric solids. In Section 2.2 one can find the explanation of this behavior based on the phenomenon of electrocapillary coupling at metal-electrolyte interfaces. Local elastic deformation at the surfaces of the internal ligament network of np-Au are caused by a macroscopic elastic straining of the specimen. A subsequent local variation of potential or charge-density is dominated by the electrocapillary coupling parameter ζ of the gold surface.

The ability of the nanoporous metal-electrolyte hybrid material to generate electric signals in response to macroscopic strain depends on the magnitude of ζ , on the net surface area, and on the efficiency with which the macroscopic deformation converts into local tangential strain at each surface segment.

In a thermodynamical description of the system for actuation and active strain sensing with np-Au, two parameters were defined to afford a quantification of the material's performance in the macroscopic picture: The effective sensing coefficient ζ^* evaluates potential variation per effective applied strain and the actuation coefficient A^* measures strain per charge in actuation. A link between the two coefficients that also involves the effective Young's modulus, Y^* , of the porous material was predicted via Eq (4.8). Each of the three parameters (ζ^* , A^* , and Y^*) were determined independently. For comparison ζ^* was measured in strain-sensing experiments (ζ_{sensing}^*) as well as calculated from A^* and Y^* ($\zeta_{\text{relation}}^*$). The results yield good agreement with Eq (4.8), since both values coincide within variance, i.e. $\zeta_{\text{sensing}}^* \approx \zeta_{\text{relation}}^*$. This confirms the previously given phenomenological description of the effective materials behavior to macroscopic deformation.

This conclusion is further validated by the comparison of the experimental value of A^* (i.e. effective strain per volumetric charge density, $d\varepsilon^*/dq^V|_F$) to the prediction in Eq (4.3): This equation connects the local electrocapillary coupling strength at the surface and the local elastic response in the bulk of the ligaments with the effective (macroscopic measurable) actuation coefficient A^* . With $K = 217 \text{ GPa}$ [72], $\Theta = 5.5$ [39],

$\varsigma = -2.0 \text{ V}$ [4–6, 63, 69] and $\varphi = 0.26$, Eq (4.3) computes A^* as $0.0433 \text{ mm}^3 \text{ C}^{-1}$. This value agrees well with the mean experimental $A^* = 0.0475 \text{ mm}^3 \text{ C}^{-1}$ determined in this work. The accordance confirms furthermore that sensing and actuation behavior are both expressions of the same microscopic coupling process. As stated before, this process is governed by the local electrocapillary coupling parameter ς .

The actuation experiments in this work used switching times of several minutes and explore therefore a quasi-static scenario. Applicable sensors require a possible charge transfer at higher frequencies. The sensing experiments performed at 20 Hz showed an effective capacity C considerably below (factor 50) the quasi-static one. The deceleration of charge transfer as a result of ionic transport in the pore space implements a natural explanation of this observation. This conclusion is also promoted by electrochemical impedance spectroscopy on np-Au [73]. The data in Table 5.1, however, show the potential variation during constant-charge sensing at 20 Hz ($\varsigma^* = \hat{E}/\hat{\varepsilon}^*|_{qV}$) in excellent agreement with the quasi-static actuation results ($\varsigma^* = -Y^*A^*$), indicating that the material provides relevant signals even at finite frequency as an active strain sensor.

Table 5.1: Effective potential-strain coupling coefficients ς^* determined in two independent ways: $\varsigma^* = \hat{E}/\hat{\varepsilon}^*|_{qV}$ is obtained from potential and strain amplitudes in sensing experiments; $\varsigma^* = -Y^*A^*$ is obtained from quasi-static actuation experiments and Young’s modulus via Eq (4.8). All sensing experiments were performed at constant potential and at a frequency of 20 Hz. Also shown: ligament size L , and solid fraction, φ , of the specimens.

	L [nm]	φ [-]	$\varsigma^* = \hat{E}/\hat{\varepsilon}^* _{qV}$ [mV]	$\varsigma^* = -Y^*A^*$ [mV]
masteralloy				
Au ₂₅ Ag ₇₅	40 ± 10	0.26	-46.4 ± 1.3	-42.8 ± 5.7

5.2 Sensing efficiency of nanoporous-metal electrolyte hybrid materials

The experimental value of ς^* for the nanoporous gold structure fabricated from an Au₂₅Ag₇₅ master alloy (ligament size of 40 nm) is found as $(-46.4 \pm 1.3) \text{ mV}$. Thus, a strain of 1 % results in a potential variation of 460 μV . Piezoceramics can reach much higher potential responses to strain than the specimens investigated in this work. Nevertheless, np-Au active strain sensors exhibit a extremely large surface area and, thus, a large electric capacity compared to piezoceramics. Consequently, a readout circuitry in a conceivable application can be designed to be comparatively inexpensive and simple, although the generated voltage is small.

Active strain sensing with np-Au yields in robust electrical responses (potential or current) as a result of the abundant active sites at the extremely large internal surface. All active sites contribute to the potential change or to the charge displacement and therefore take part in the electric response. In order to verify this statement the results of the experiments on np-Au are compared to a high performance piezoceramic, see summary in Fig. 5.1.

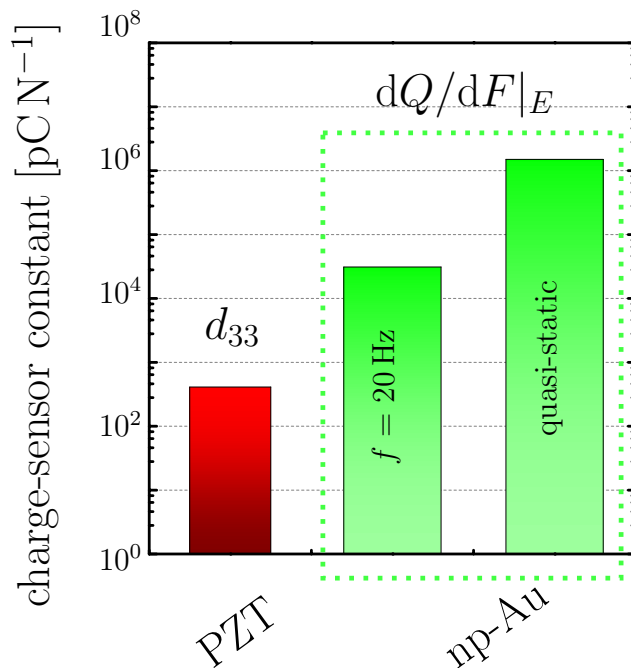


Figure 5.1: Comparing the charge-load response of nanoporous gold- (np-Au-) based hybrid material to that of lead zirconium titanate (PZT). The response $dQ/dF|_E$ of np-Au at frequency 20 Hz is 75 fold larger than the piezoelectric charge-sensor constant d_{33} of PZT [74]. Under quasi-static conditions, $dQ/dF|_E$ of np-Au is even higher, almost 4000 fold larger than d_{33} of PZT. Graph adapted from Stenner *et al.*, see Ref. [42].

A suitable parameter for comparison is the piezoelectric charge-sensor constant d_{33} in longitudinal direction. For lead zirconium titanate (PZT, here: $(\text{Pb}_{0.85}\text{Ba}_{0.15})_{0.9925}\text{La}_{0.005}(\text{Zr}_{0.52}\text{Ti}_{0.48})\text{O}_3$) d_{33} is found to be 410 pCN^{-1} [74]. In quasi-static measurements with our material yield a mean (averaged over three samples) longitudinal coupling parameter of $dQ/dF|_E = 1.5 \text{ pCN}^{-1}$. This value is almost 4000 times larger than d_{33} of PZT. Whereas at a frequency of 20 Hz, $dQ/dF|_E = 31 \text{ nCN}^{-1}$, is fifty fold less, but nevertheless almost two orders of magnitude larger than d_{33} of PZT. However, even at finite frequencies like 20 Hz one can tailor the longitudinal coupling parameter, and therewith the electric response of np-Au the sensor: $dQ/dF|_E$ scales with the thickness. By contrast, d_{33} is a materials' constant of a piezoceramic composition and

cannot be tailored by the design of the sensor geometry. Near equilibrium the coupling between net charge on the sample and external load was investigated in quasi-static sensing experiments at frequency of 10 mHz. Nanoporous-metal based sensors and actuators display similar phenomenological behavior as piezoelectric solids. As discussed above, the performance is not in all details identical. Nevertheless, phenomenologically, in both materials a mechanical deformation generates voltage or electric charge, and conversely an applied potential or charge generate mechanical deformation.

However, the underlying microscopic mechanisms are very different. In piezoelectric crystals symmetry-breaking strain that displaces electric charge in each crystallographic unit cell is induced by the applied load. Via this displacement the lattice becomes polarized and thus charge accumulates at the *external* sample surface. By contrast, as described in Sec. 2.2, straining of the porous metal network leads to a change in chemical potential of the conduction electrons [6]. The entire *internal* electrode surface has then to be polarized to counterbalance this change and to maintain the electrode potential a constant. In order to create space-charge layers at internal interfaces throughout the porous material long-range charge transport is required. Unfortunately, long-range charge transport limits the sensing efficiency at elevated frequency. However, as shown for the frequency range explored in this work there is no such considerable limitation: Up to an applied frequency $f = \omega/2\pi$ of 100 Hz the electric responses stay constant, although the transferred charge decreases. Regardless of the applied frequency, the large number of internal interfaces entails that the net amount of charge which is transferred in nanoporous metal sensors in response to strain is much larger than the charge displayed in piezoceramics.

5.3 Local and macroscopic strain

There is an ongoing discussion in the community about the influence of ligament size and connectivity density on the mechanical properties of nanoporous gold (see e.g. Refs. [10, 33, 47, 48]). Due to the so-called dangling ligaments in a structure with less network connectivity density (i.e. less load-bearing ligaments within the specimen) one expects a higher stiffness and strength than the mechanical parameters that are actually observed. Thus, stiffness and strength are predicted to increase with increasing connectivity density [47]. This prediction coincides with the observed increase in effective Young's modulus Y^* with increasing connectivity density in this work.

Furthermore the ability of sensing or actuation with nanoporous metal depends on how macroscopic strain couples into local strain at the surfaces of the ligaments. Table 5.1 points towards a surprising effect: For a higher connected network of ligaments (specimens A) we did not observe as expected a higher potential-strain coupling parameter ζ^* but a

similar one. This is unexpected, since specimen *A* exhibits smaller ligaments (30 nm) and a higher solid fraction $\varphi \approx 0.3$ compared to *B* ($L = 40$ nm and $\varphi \approx 0.26$) while having the same macroscopic size. One would expect that $|\zeta_A^*| \geq |\zeta_B^*|$ since one might expect that a higher number of load bearing paths should lead to a higher number of strained ligaments and therefore to an increased surface stress at the same effective applied strain $\hat{\epsilon}^*$. However, the distribution of surface stresses in a nanoporous network is complicated as many factors can affect surface stress.

The link between local and macroscopic elastic behavior of np-Au has been debated with regards of scaling relations [9,75]. One scaling relation, the Gibson-Ashby scaling relation, for porous solids concerning the Young's modulus is $Y^* = Y\varphi^2$, where Y expresses the Young's modulus of the solid phase [46]. The Gibson-Ashby scaling relation and Eq (4.3) can be inserted into Eq (4.8), thus, with $Y = 3K(1 - 2\nu)$ for isotropic elastic media, one obtains the following prediction for the effective potential-strain response parameter:

$$\zeta^* = \frac{2}{3}(1 - 2\nu)\Theta_\zeta\varphi \quad (5.1)$$

With $\nu = 0.44$ [72] and with the values of ζ and φ as in Sec. 5.1, Eq (5.1) yields $\zeta^* = -240$ mV, for specimens *B* ($\varphi = 0.26$) and -280 mV for specimens *A* ($\varphi = 0.3$). These values are about 5 fold larger than the experimental value. In this case, however, the discrepancy is expected, considering that the scaling relations overestimate the stiffness of macroscopic np-Au samples more than by a factor of ten [16].

Another scaling relation for nanoporous networks is proposed by Soyarslan *et al.*, in Ref. [48] via finite element simulations. This scaling relation is modified from the one that Roberts and Garboczi suggested in Ref. [76] and takes systematic changes in connectivity density into account. The relation emerges as $Y^* = YC_2 \left[\frac{\varphi - \Phi_B^P}{1 - \Phi_B^P} \right]^m$ with a correlation function $C_2 = 2.03$, the percolation threshold $\Phi_B^P = 0.159$, and $m = 2.56$. m and C_2 have been determined via linear regression. By inserting the scaling relation and Eq (4.3) into Eq (4.8) (analogously to the discussion of the Gibson-Ashby scaling relation) the following prediction for the effective potential-strain response parameter is obtained:

$$\zeta^* = \frac{2}{3}(1 - 2\nu)\Theta_\zeta \frac{C_2}{\varphi} \left[\frac{\varphi - \Phi_B^P}{1 - \Phi_B^P} \right]^m \quad (5.2)$$

With the values as stated above ζ^* emerges from Eq. (5.2) as -60 mV, for specimens *A* and -30 mV for specimens *B*, which is in the same order of magnitude as the experimental values. Thus, the modified scaling relation from Soyarslan *et al.* leads to a better agreement between theory and experiment than the Gibson-Ashby scaling relation.

Dangling ligaments, that do not cooperate in the deformation of the loadbearing paths within the solid network, have been suggested as the origin of the discrepancy between

Gibson-Ashby and the macroscopic behavior of np-Au [10]. This suggests that by improving the connectivity density of the nanoporous solids up to an *ideally* interconnected network of ligaments one could tailor the sensing efficiency and thus theoretically increase it fivefold. Theoretically, one more method to enhance the sensing efficiency is to increase the solid fraction. With regard to Eq (5.1) and Eq. (5.2), increasing φ improves the electromechanical coupling, as well as the mechanical strength, since a higher solid fraction also implies a higher mechanical strength. Both are desirable for applications.

Following Refs. [15, 16, 45, 77–79]¹ a qualitative discussion of the influence of structural properties as connectivity density and ligament size will be given here:

Capillary forces drive a local yielding even in the absence of external load [16, 77, 78]. Thus, as-prepared specimens exhibit lattice defects depending on the synthesis and structure size. The influence of each preparation protocol on lattice effects has not been evaluated.

The elastic behavior of a nanoporous specimen under uniaxial compression may be governed by ligament bending. Thus, one part of the ligament surfaces are strained in compression while others are in tension. The corresponding induced electric signals would partly cancel out each other. Furthermore, the node thickness or the *ligament length* affects the tendency of torsion of a ligament under load. The longer the ligaments, the more torque is created. This implies that not only the thickness of the ligament but also structural parameters account for different surface stresses [15].

During compression of a comparable nanoporous gold specimen as *B* ($\varphi \approx 0.26$) a continuous loss of free surface was observed. Although most of the surface reduction was found at higher strains than in the experiments presented in this thesis, ($\varepsilon_{\text{true}} \geq 0.1 \approx \varepsilon^*$), during pre-deformation strains of 0.15 were reached. The loss of surface area during straining is on account of cold coalescence of ligaments. Compression pushes ligaments towards each other, thus, some of them will touch and coalesce at surface sites [79]. One might expect this will happen at lower strains for higher solid fraction networks (i.e. specimens *A* with $\varphi = 0.3$), since there is more solid material at same volume, i.e. less distance between each ligament. This might lead to a decrease in surface area at lower strains. Cold coalescence might also improve the connectivity density of the lower solid fraction samples.

However, these observations aim at different effects and base mainly on finite element and atomistic simulations (e.g. Refs. [15, 16]). One has to be very careful to transfer the results one to one to the experiments performed in this work.

This study shows, however, that even via an increased solid fraction and smaller ligament

¹Most of the studies focus on the influence of surface stress on Young’s modulus, yield stress or compliance, not vice versa. Nevertheless, surface stress and these parameters are interconnected, thus it is sufficient for a qualitative discussion.

size L , which lead to more mechanical strength and higher connectivity density, the effective potential-strain response parameter could not be enhanced, but remained constant (see table 5.2).

Table 5.2: Effective potential-strain coupling coefficients ζ^* obtained from sensing experiments for three different sample types. All sensing experiments were performed at constant potential and at a frequency of 20 Hz. Also shown: solid fraction, φ , net capacity, C , net surface area, S , and residual silver amount of each sample.

<i>denomination,</i> master alloy, ligament size	ζ^* [mV]	φ [-]	C [mF]	S [cm ²]	residual silver [at.%]
<i>A</i> , Au ₃₀ Ag ₇₀ , 30 nm	-49.0 ± 0.6	0.30	48 ± 2	1200	≈ 5
<i>B</i> , Au ₂₅ Ag ₇₅ , 40 nm	-46.4 ± 1.3	0.26	51 ± 3	1280	≤ 1
<i>C</i> , Au ₂₅ Ag ₇₅ , 100 nm	-5.0 ± 1.0	0.26	15 ± 3	370	≤ 1

Nevertheless, the specimens with a high solid fraction ($\varphi \approx 0.3$) investigated in this work exhibit a higher amount of residual silver (5 at.%) than the other samples. Although energy-dispersive X-ray spectroscopy does not support information whether the Ag-atoms are located in the bulk or at the surface of the np-Au, the unexpected small capacitance C point towards a change in surface properties that could lead to a decrease in C , S , and ζ^* (comparison between specimens *A* and *B*, see table 5.2).

6 Summary and Outlook

This work demonstrates the proof-of-principle for active strain-sensing with a hybrid material made of a nanoscaled-gold skeleton and electrolyte. Via cyclic deformation of mm-sized specimens robust and reproducible electrical signals that are measurable without further amplification were obtained. Three different types of nanoporous gold (np-Au) samples were investigated: the connectivity density and ligament size, L , was varied between them. The potential- and current responses of the specimen with different sample characteristics increase linearly with the applied macroscopic strain. The effective potential-strain coupling parameter is determined as $\zeta^* = dE/d\varepsilon^*|_q^V \approx -50$ mV for samples with comparable structure size ($L = 30 - 40$ nm) but different connectivity density. Increasing the ligament size to 100 nm leads to a decrease of ζ^* by a factor of 10. The frequency $f = \omega/2\pi$ within the range of 0.5 to 100 Hz exploited in this work showed a negligible influence on current and potential responses, the transferred charge, however, decreased with increasing f .

A macroscopic sensing-actuation relation, Eq (4.8), is derived from phenomenological thermodynamics. This relation leads to excellent agreement with the experimental results from sensing, actuation, and elasticity measurements. The basis of the analysis of the material's behavior is the electrocapillary coupling at the pore surfaces in the material. The sensing efficiency represented via ζ^* is consistent with the prediction based on that concept.

The charge-load coupling coefficient of the nanoporous gold-electrolyte hybrid material, $dQ/dF|_E$, can reach values that are several orders of magnitude higher than the equivalent parameter, d_{33} , of a high performance piezoceramic. Thus, the np-Au sensor is capable of generating significant electric current in response to strain as a result of its extremely large internal surface area.

Although the microscopic nature of the charge-load response differ between a nanoporous metal and conventional piezoelectric solids, charge couples to load, and elastic strain creates polarization in each case. Moreover, the macroscopic phenomenology of piezoelectricity, i.e. the displacement of charge induced by an external load, is the same in both materials. Since nanoporous metals exhibit particularly robust signals, this class of materials might be an easily imaginable alternative for piezoceramics as active strain-sensing

components with high strain-induced charge densities.

By replacing gold with a more affordable metal the sensor will become cheaper while the synthesis process of nanoporous-metal hybrid materials is straightforward and might make this class of material attractive for future applications. Nevertheless, a clean surface is crucial for the functionality of the sensor. Even a small amount of residual silver (≈ 5 at.%) might be the reason for an impaired sensing efficiency, thus one has to evaluate possible materials carefully.

Another route to increase the sensing and actuation ability of the material is the introduction of a polymer-layer to the metal skeleton, as shown in Ref. [23] by Wang, Stenner and Weißmüller. Via maintaining a well-defined gold surface covered with polypyrrole (PPy) the actuation efficiencies could be increased considerably, see Fig. 6.1.

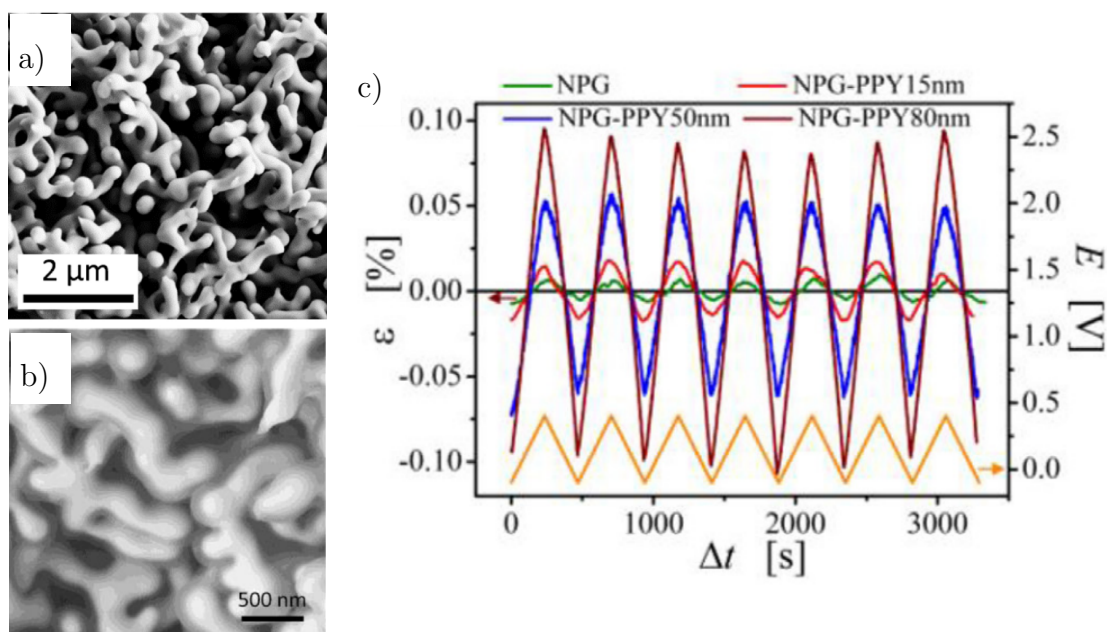


Figure 6.1: The actuation efficiency can be tuned via coating the nanoporous metal surface with a polymer (here: polypyrrole, PPy). SEM micrographs a) and b) show the nanoporous gold structure with a ligament size of (250 ± 50) nm without PPy and with a (80 ± 20) nm thick PPy layer, respectively. c) Actuation experiments performed on np-Au sample shown in a) (green line) and b) (brown line). By covering the structure with 80 nm PPy, the observed effective strain in actuation could be enhanced by a factor of 12. Red and blue lines correspond to actuation signals obtained from samples covered with a 15 nm and 50 nm thick PPy layer, respectively. The yellow line indicates the applied potential. Graphics adapted from K. Wang, C. Stenner, and J. Weissmüller, *Sensors and Actuators B: Chemical*, 248:622-629, 2017 with permission from Elsevier.

Additionally, the induced strain amplitude increases linearly with the thickness of the PPy layer. Therefore, one can increase the actuation efficiency furthermore via a thicker PPy layer. The actuation coefficient $A^* = d\varepsilon^*/dqV|_T$ was calculated as

$(0.0675 \pm 0.0004) \text{ mm}^3 \text{ C}^{-1}$ for a layer thickness of 80 nm, which is higher than the value obtained from pure nanoporous gold in this work, $A^* = (0.0475 \pm 0.0010) \text{ mm}^3 \text{ C}^{-1}$.

To increase the lifetime of the nanoporous-metal hybrid material sensor, one might consider to alloy Au with Pt, since Pt is known to stabilize the structure of nanoporous AuPt against coarsening and to inhibit the surface area reduction [11, 12]. However, a constant sensing and actuation efficiency was found after 1.2×10^5 load cycles in sensing plus 25 actuation cycles performed in this work.

References

- [1] A.Ya. Gokhshtein. Charge acquirement by an elastically strained electrode. *Doklady Akademii Nauk Sssr*, 187(3):601, 1969.
- [2] J. Weissmüller and D. Kramer. Balance of force at curved solid metal-liquid electrolyte interfaces. *Langmuir*, 21(10):4592–4603, 2005.
- [3] M. Smetanin, R. N. Viswanath, D. Kramer, D. Beckmann, T. Koch, L. A. Kibler, D. M. Kolb, and J. Weissmüller. Surface stress-charge response of a (111)-textured gold electrode under conditions of weak ion adsorption. *Langmuir*, 24(16):8561–8567, 2008.
- [4] M. Smetanin, D. Kramer, S. Mohanan, U. Herr, and J. Weissmüller. Response of the potential of a gold electrode to elastic strain. *Physical Chemistry Chemical Physics*, 11(40):9008–9012, 2009.
- [5] M. Smetanin, Q. Deng, and J. Weissmüller. Dynamic electro-chemo-mechanical analysis during cyclic voltammetry. *Physical Chemistry Chemical Physics*, 13:17313–17322, 2011.
- [6] Y. Umeno, C. Elsässer, B. Meyer, P. Gumbsch, M. Nothacker, J. Weissmüller, and F. Evers. Ab initio study of surface stress response to charging. *Europhysics Letters*, 78(1):13001, 2007.
- [7] R. Li and K. Sieradzki. Ductile-brittle transition in random porous au. *Physical Review Letters*, 68:1168–1171, 1992.
- [8] J. Erlebacher, M. J. Aziz, A. Karma, N. Dimitrov, and K. Sieradzki. Evolution of nanoporosity in dealloying. *Nature*, 410(6827):450–453, 2001.
- [9] J. Weissmüller, R. C Newman, Hai-Jun Jin, A. M. Hodge, and J. W. Kysar. Nanoporous metals by alloy corrosion: Formation and mechanical properties. *MRS Bulletin*, 34:577, 2009.

- [10] N. Mameka, K. Wang, J. Markmann, E. T. Lilleodden, and J. Weissmüller. Nanoporous Gold—Testing Macro-scale Samples to Probe Small-scale Mechanical Behavior. *Materials Research Letters*, 3831:1–10, 2015.
- [11] J. Snyder, P. Asanithi, A. B. Dalton, and J. Erlebacher. Stabilized nanoporous metals by dealloying ternary alloy precursors. *Advanced Materials*, 20(24):4883–4886, 2008.
- [12] H. J. Jin, X. L. Wang, S. Parida, K. Wang, M. Seo, and J. Weissmüller. Nanoporous Au-Pt alloys as large strain electrochemical actuators. *Nano Letters*, 10(1):187–194, 2010.
- [13] M. T. McDowell, A. M. Leach, and K. Gall. Bending and tensile deformation of metallic nanowires. *Modelling and Simulation in Materials Science and Engineering*, 16(4):045003, 2008.
- [14] J. Weissmüller, R. N. Viswanath, D. Kramer, P. Zimmer, R. Würschum, and H. Gleiter. Charge-induced reversible strain in a metal. *Science*, 300(5617):312–315, 2003.
- [15] N. Huber, R.N. Viswanath, N. Mameka, J. Markmann, and J. Weißmüller. Scaling laws of nanoporous metals under uniaxial compression. *Acta Materialia*, 67:252 – 265, 2014.
- [16] B.-N. D. Ngô, A. Stukowski, N. Mameka, J. Markmann, K. Albe, and J. Weissmüller. Anomalous compliance and early yielding of nanoporous gold. *Acta Materialia*, 93(0):144–155, 2015.
- [17] V. Zielasek, B. Jürgens, C. Schulz, J. Biener, M. M. Biener, A. V. Hamza, and M. Bäumer. Gold catalysts: Nanoporous gold foams. *Angewandte Chemie International Edition*, 45(48):8241–8244, 2006.
- [18] C. Xu, J. Su, X. Xu, P. Liu, H. Zhao, F. Tian, and Y. Ding. Low temperature co oxidation over unsupported nanoporous gold. *Journal of the American Chemical Society*, 129(1):42–43, 2007. PMID: 17199279.
- [19] A. Wittstock, J. Biener, and M. Bäumer. Nanoporous gold: a new material for catalytic and sensor applications. *Physical Chemistry Chemical Physics*, 12:12919–12930, 2010.
- [20] M. Graf, M. Haensch, J. Carstens, G. Wittstock, and J. Weissmüller. Electrocatalytic methanol oxidation with nanoporous gold: microstructure and selectivity. *Nanoscale*, 9:17839–17848, 2017.

-
- [21] J. Weissmüller and J. W. Cahn. Mean stresses in microstructures due to interface stresses: A generalization of a capillary equation for solids. *Acta Materialia*, 45(5):1899–1906, 1997.
- [22] E. Detsi, P. Onck, and J. Th. M. De Hosson. Metallic muscles at work: High rate actuation in nanoporous gold/polyaniline composites. *ACS Nano*, 7(5):4299–4306, 2013.
- [23] K. Wang, C. Stenner, and J. Weissmüller. A nanoporous gold-polypyrrole hybrid nanomaterial for actuation. *Sensors and Actuators B: Chemical*, 248:622 – 629, 2017.
- [24] F. Weigend, J. Weissmüller, and F. Evers. Structural relaxation in charged metal surfaces and cluster ions. *Small*, 2(12):1497–1503, 2006.
- [25] E. Detsi, Marc S. Sellès, P. R. Onck, and J. Th M. De Hosson. Nanoporous silver as electrochemical actuator. *Scripta Materialia*, 69(2):195–198, 2013.
- [26] C. Cheng and A. H. W. Ngan. Reversible electrochemical actuation of metallic nanohoneycombs induced by pseudocapacitive redox processes. *ACS Nano*, 9(4):3984–3995, 2015.
- [27] S. B. Lang. Guide to the literature of piezoelectricity and pyroelectricity. 27. *Ferroelectrics*, 350(1):124–239, 2007.
- [28] N.A. Pertsev A.L. Kholkin and A.V. Goltsev. *Piezoelectricity and Crystal Symmetry*, pages 17–38. Springer Science+Business Media, LLC, New York, USA, 2008.
- [29] J. Erhart. Experiments to demonstrate piezoelectric and pyroelectric effects. *Physics Education*, 48(4):438, 2013.
- [30] A. Ballato. Piezoelectricity: history and new thrusts. In M.Schneider Levy and B.R. S.C. McAvoy, editors, *Ultrasonics Symposium 1996*, volume 1, pages 575–583, San Diego, 1996. IEEE.
- [31] S. Shi, J. Markmann, and J. Weissmüller. Synthesis of uniform bulk nanoporous palladium with tunable structure. *Electrochimica Acta*, 285:60 – 69, 2018.
- [32] J. Biener, A. M. Hodge, J. R. Hayes, C. A. Volkert, L. A. Zepeda-Ruiz, A. V. Hamza, and F. F. Abraham. Size effects on the mechanical behavior of nanoporous au. *Nano Letters*, 6(10):2379–2382, 2006.

- [33] L. Lührs, C. Soyarslan, J. Markmann, S. Bargmann, and J. Weissmüller. Elastic and plastic poisson ' s ratios of nanoporous gold. *Scripta Materialia*, 110:65–69, 2016.
- [34] H.-J. Jin, S. Parida, D. Kramer, and J. Weissmüller. Sign-inverted surface stress-charge response in nanoporous gold. *Surface Science*, 602(23):3588–3594, 2008.
- [35] L. Lührs and J. Weissmüller. Nanoporous copper-nickel – macroscopic bodies of a strong and deformable nanoporous base metal by dealloying. *Scripta Materialia*, 155:119 – 123, 2018.
- [36] I. V. Okulov, J. Weissmüller, and J. Markmann. Dealloying-based interpenetrating-phase nanocomposites matching the elastic behavior of human bone. *Scientific Reports*, 7(20), 2017.
- [37] A.J. Bard and L.R. Faulkner. *Electrochemical methods: fundamentals and applications*. Wiley VCH, Weinheim, Germany, 2001.
- [38] J. Weissmüller. *Electrocapillarity of Solids and its Impact on Heterogeneous Catalysis*, pages 163–219. Adv. Electrochem. Sci. Eng. Wiley VCH, Weinheim, Germany, 2013.
- [39] J. Weissmüller, H.-L. Duan, and D. Farkas. Deformation of solids with nanoscale pores by the action of capillary forces. *Acta Materialia*, 58(1):1 – 13, 2010.
- [40] R. Shuttleworth. The surface tension of solids. *Proceedings Royal Phys. Soc. A*, 63(365):444–457, 1950.
- [41] A. Michl, J. Weissmüller, and S. Müller. Electrocapillary Coupling at Metal Surfaces from First Principles: On the Impact of Excess Charge on Surface Stress and Relaxation. *Langmuir*, 34(16):4920–4928, 2018.
- [42] C. Stenner, L.-H. Shao, N. Mameka, and J. Weissmüller. Piezoelectric gold: Strong charge-load response in a metal-based hybrid nanomaterial. *Advanced Functional Materials*, 26(28):5174–5181, 2016.
- [43] J. Erlebacher. Evaluation and origins of the difference between double-layer capacitance behaviour at au-metal and oxidized au surfaces. *Journal of The Electrochemical Society*, 151:C614–C626, 2004.
- [44] K. Wang, A. Kobler, C. Kübel, H. Jelitto, G. Schneider, and J. Weissmüller. Nanoporous-gold-based composites: toward tensile ductility. *NPG Asia Materialia*, 7:e187, 2015.

-
- [45] K.R. Mangipudi, E. Epler, and C.A. Volkert. Morphological similarity and structure-dependent scaling laws of nanoporous gold from different synthesis methods. *Acta Materialia*, 140:337 – 343, 2017.
- [46] L. J. Gibson and M. F. Ashby. *Cellular Solids*. Pergamon Press, Oxford, 2nd edition, 1999.
- [47] L.-Z. Liu, X.-L. Ye, and H.-J. Jin. Interpreting anomalous low-strength and low-stiffness of nanoporous gold: Quantification of network connectivity. *Acta Materialia*, 118:77 – 87, 2016.
- [48] C. Soyarslan, S. Bargmann, M. Pradas, and J. Weissmüller. 3d stochastic bicontinuous microstructures: Generation, topology and elasticity. *Acta Materialia*, 149:326–340, 2018.
- [49] Metrohm Autolab. *NOVA Getting Started*.
- [50] Z. Wang, S. Ning, P. Liu, Y. Ding, A. Hirata, T. Fujita, and M. Chen. Tuning surface structure of 3d nanoporous gold by surfactant-free electrochemical potential cycling. *Advanced Materials*, 29(41):1703601.
- [51] B. E. Conway. Electrochemical oxide film formation at noble-metals as a surface-chemical process. *Progress in Surface Science*, 49(4):331–452, 1995.
- [52] H. Keiser, K.D. Beccu, and M.A. Gutjahr. Abschätzung der porenstruktur poröser elektroden aus impedanzmessungen. *Electrochimica Acta*, 21(8):539 – 543, 1976.
- [53] E. McCafferty. *Introduction to Corrosion Science*. Springer Science+Business Media, New York Dordrecht Heidelberg London, 2010.
- [54] Metrohm Autolab. *NOVA Impedance Spectroscopy Tutorial*.
- [55] J.O’M. Bockris, Reddy A.K.N., and M. Gamboa-Aldeco. *Modern electrochemistry, second edition, fundamentals of electrodicts*. Kluwer Academic Publishers, New York, Boston, Dordrecht, London, Moscow, 2nd edition, 2002.
- [56] Stanford Research Systems. *DSP Lock-In Amplifier model SR830*. SRS.
- [57] Netzsch. *Operating Instructions DMA 242 C*.
- [58] K.P. Menard. *Dynamic Mechanical Analysis*. CRC Press LLC, Boca Raton, USA, 1999.

- [59] O. Kraft, P. A. Gruber, R. Mönig, and D. Weygand. Plasticity in Confined Dimensions. *Annual Review of Materials Research*, 40(1):293–317, 2010.
- [60] B. N.D. Ngô, B. Roschning, K. Albe, J. Weissmüller, and J. Markmann. On the origin of the anomalous compliance of dealloying-derived nanoporous gold. *Scripta Materialia*, 130:74–77, 2017.
- [61] S. Trasatti and O. A. Petrii. Real surface-area measurements in electrochemistry. *Pure and Applied Chemistry*, 63(5):711–734, 1991.
- [62] P. S. Germain, W. G. Pell, and B. E. Conway. Evaluation and origins of the difference between double-layer capacitance behaviour at au-metal and oxidized au surfaces. *Electrochimica Acta*, 49(11):1775 – 1788, 2004.
- [63] M. C. Lafouresse, U. Bertocci, C. R. Beauchamp, and G. R. Stafford. Simultaneous Electrochemical and Mechanical Impedance Spectroscopy Using Cantilever Curvature. *Journal of the Electrochemical Society*, 159(10):H816–H822, 2012.
- [64] Z. Shi, J. Lipkowski, M. Gamboa, P. Zelenay, and A. Wieckowski. Investigations of SO_4^{2-} adsorption at the au(111) electrode by chronocoulometry and radiochemistry. *Journal of Electroanalytical Chemistry*, 366(1-2):317–326, 1994.
- [65] H. B. Callen. *Thermodynamics and an Introduction to Thermostatistics, 2nd Edition*. Wiley, 1985.
- [66] J. Sirohi and I. Chopra. Fundamental Understanding of Piezoelectric Strain Sensors. *Journal of Intelligent Material Systems and Structures*, 11(4):246–257, 2000.
- [67] H.-J. Jin and J. Weissmüller. Bulk nanoporous metal for actuation. *Advanced Engineering Materials*, 12(8):714–723, 2010.
- [68] L. H. Shao, H. J. Jin, R. N. Viswanath, and J. Weissmüller. Different measures for the capillarity-driven deformation of a nanoporous metal. *Europhysics Letters*, 89(6):66001, 2010.
- [69] Q. Deng and J. Weissmüller. Electrocapillary coupling during electrosorption. *Langmuir*, 30(34):10522–10530, 2014.
- [70] X. Y. Lang, H. T. Yuan, Y. Iwasa, and M. W. Chen. Three-dimensional nanoporous gold for electrochemical supercapacitors. *Scripta Materialia*, 64(9):923–926, 2011.
- [71] K. Hu, M. Ziehmer, K. Wang, and E. T. Lilleodden. Nanoporous gold: 3d structural analyses of representative volumes and their implications on scaling relations of mechanical behaviour. *Philosophical Magazine*, 96(32-34):3322–3335, 2016.

-
- [72] G.W.C. Kaye and T.H. Laby. *Tables of Physical and Chemical Constants*. Longman, 1995.
- [73] S. Cattarin, D. Kramer, A. Lui, and M. M. Musiani. Preparation and characterization of gold nanostructures of controlled dimension by electrochemical techniques. *Journal of Physical Chemistry C*, 111(34):12643–12649, 2007.
- [74] Y. Saito, H. Takao, T. Tani, T. Nonoyama, K. Takatori, T. Homma, T. Nagaya, and M. Nakamura. Lead-free piezoceramics. *Nature*, 432(November):84–87, 2004.
- [75] A. M. Hodge, R. T. Doucette, M. M. Biener, J. Biener, O. Cervantes, and A. V. Hamza. Ag effects on the elastic modulus values of nanoporous au foams. *Journal of Materials Research*, 24(4):1600–1606, 2009.
- [76] A. P. Roberts and E. J. Garboczi. Computation of the linear elastic properties of random porous materials with a wide variety of microstructure. *Proceedings of the Royal Society A: Mathematical, Physical and Engineering Sciences*, 458(2021):1033–1054, 2002.
- [77] S. Parida, D. Kramer, C. A. Volkert, H. Rosner, J. Erlebacher, and J. Weissmüller. Volume change during the formation of nanoporous gold by dealloying. *Physical Review Letters*, 97(3):035504, 2006.
- [78] D. A. Crowson, D. Farkas, and S.G. Corcoran. Mechanical stability of nanoporous metals with small ligament sizes. *Scripta Materialia*, 61(5):497 – 499, 2009.
- [79] D.-B. N. Ngo. *Elasticity and plasticity of nanoporous gold: implications of molecular dynamics simulations*. PhD thesis, Hamburg University of Technology, 2017.